1 **Title**

2 Roles of the ClC Chloride Channel CLH-1 in Food-associated Salt Chemotaxis Behavior of *C.*

3 *elegans*

4

5 **Author names and affiliations**

6 Chanhyun Park[1], Yuki Sakurai[1], Hirofumi Sato[1], Shinji Kanda[1, 2], Yuichi Iino[1], Hirofumi

7 Kunitomo[1]

8

9 1 Department of Biological Sciences, School of Science, The University of Tokyo, Tokyo, Japan

10 2 Laboratory of Physiology, Atmosphere and Ocean Research Institute, The University of

11 Tokyo, Chiba, Japan

12

Abstract

The ability of animals to process dynamic sensory information facilitates foraging in an ever changing environment. However, molecular and neural mechanisms underlying such ability remain elusive. The ClC anion channels/transporters play a pivotal role in cellular ion homeostasis across all phlya. Here we find a ClC chloride channel is involved in salt concentration chemotaxis of *C. elegans*. Genetic screening identified two altered-function mutations of *clh-1* that disrupt experience-dependent salt chemotaxis. Using genetically encoded fluorescent sensors, we demonstrate that CLH-1 contributes to regulation of chloride and calcium dynamics of salt-sensing neuron, ASER. The mutant CLH-1 reduced responsiveness of ASER to salt stimuli in terms of both temporal resolution and intensity, which could disrupt navigation strategies for approaching preferred salt concentration. Furthermore, other ClC genes appeared to act redundantly in salt chemotaxis. These findings provide insights into the regulatory mechanism of neuronal responsivity by ClCs that contribute to modulation of navigation behavior.

Introduction

Memorizing environmental conditions associated with food and generating an optimal foraging strategy based on those memories are basic and important abilities for survival. Mechanisms of food-associated learning have long been addressed in many species, dating back to Pavlovian appetitive conditioning demonstrated in dogs (Braubach et al., 2009; Cho et al., 2016; Gottfried et al., 2003; Hirano et al., 2013; O'Doherty et al., 2003; Otis et al., 2017; Pavlov, 1927; Sasakura and Mori, 2013; Winter and Stich, 2005). By virtue of its simple nervous system and amenability to genetic manipulations, the soil nematode *Caenorhabditis elegans* has been used to unveil molecular and neural mechanisms of learning. *C. elegans* shows food-associated learning in combination with various sensory modalities including gustatory, olfactory, thermosensory, and mechanosensory cues (Colbert and Bargmann, 1995; Hedgecock and Russell, 1975; Kindt et al., 2007; Saeki et al., 2001). We have previously reported that *C. elegans* shows plasticity in chemotaxis to salt (sodium chloride; NaCl); wild-type animals are attracted to the salt concentration at which they have been fed, while avoiding concentrations at which they have been starved (salt concentration chemotaxis, Kunitomo et al., 2013, Figure 1**a**). *C. elegans* senses inorganic ions mainly through the bilateral salt-sensing neuron pair, ASE (Bargmann and Horvitz, 1991). Sensory input to ASE-right (ASER), is essential and sufficient for food-associated salt chemotaxis. Modulation of synaptic transmission from ASER to the first layer interneurons AIA, AIB and AIY, whose activity regulates exploratory behaviors (Gray et al., 2005; Li et al., 2014; Piggott et al., 2011), is also implicated in modification of salt chemotaxis (Kunitomo et al., 2013; Luo et al., 2014; Wang et al., 2017).

Molecular mechanisms that regulate perception and propagation of salt stimuli in ASER have been proposed. A receptor-type guanylyl cyclase GCY-22 plays a pivotal role in perception of salt stimuli and is suggested to act as an ion receptor of ASER (Adachi et al., 2010; Ortiz et al., 2009; Smith et al., 2013). Excitation of ASER depends also on cyclic nucleotide-gated (CNG) channels consisting of TAX-2 and TAX-4 (Suzuki et al., 2008). *C. elegans* genome does not contain typical voltage-gated sodium channel genes (Bargmann, 1998). Instead, voltage-gated calcium channels are responsible for propagation of depolarization, which is examined by electrophysiological studies (Goodman et al., 1998; Shindou et al., 2019). However, contribution of anions to the regulation of ASER activity has not been discussed yet.

Anion transporters play critical roles in regulating excitability of neurons as they finely tune electrophysiological properties of membranes. However, how and which molecules contribute to the responsivity of specific neurons and eventually produces behavioral output, remains rudimentary. Here, we identify the ClC chloride channel CLH-1 as a possible regulator of food-associated salt chemotaxis in *C. elegans*. ClC proteins transport univalent anions across membranes to control electrochemical potential of excitable cells and to maintain ionic milieu as well as pH of intracellular organelles (Ahnert-Hilger and Jahn, 2011; Bösl et al., 2001; Branicky et al., 2014). Malfunction of ClC genes results in various diseases such as myotonia, leukodystrophy, hyperaldosteronism and epilepsy in humans (Blanz et al., 2007; Charlet-B. et al., 2002; Fernandes-Rosa et al., 2018; Yamamoto et al., 2015). The causal relationship among ClC malfunction, physiological consequences, and disease manifestations are not fully understood in many cases. CLH-1 shares the highest (37%) identity with mammalian ClC-2. Functional studies using heterologous expression in *Xenopus* oocytes and mammalian cells demonstrated that both CLH-1 and ClC-2 are inwardly rectifying chloride channels (Grant et al.,

2015; Nehrke et al., 2000; Staley et al., 1996; Thiemann et al., 1992). On the other hand, two recent studies showed that ClC-2 contributes to Cl^- influx in neurons depending on the electrochemical potential of Cl^- (Ratté and Prescott, 2011; Rinke et al., 2010). Thus, the function of CLH-1/ClC-2 in the nervous system remains elusive.

In this study, we show two novel missense mutations in *clh-1* change NaCl concentration preference of *C. elegans* only after food experience. Genetic analyses revealed that CLH-1 acts in ASER and that both appropriate quantitative and spatial function of CLH-1 is required for normal low-salt chemotaxis. Functional imaging of neurons indicated that mutations in *clh-1* altered the responsivity of ASER and AIB neurons, which may consequently affect behavioral outputs. These results suggest that responsivity of the salt circuit is maintained by CLH-1 to generate proper navigation behavior in salt chemotaxis.

Results

Missense mutations of *clh-1* give rise to a disorder in food-associated salt concentration chemotaxis

C. elegans is attracted to the salt concentration at which they have been fed, while they avoid concentrations at which they have been starved (Figure 1**a** and Figure 1—figure supplement 1**a**). To better understand the molecular mechanisms of salt chemotaxis plasticity, we screened for mutants that showed defects in salt chemotaxis after feeding but not after starvation (See Materials and methods, Figure 1—figure supplement 1**b**). Two mutants, JN572 and JN577, showed a similar phenotype: impaired chemotaxis toward low salt after feeding on NaCl-free nematode growth medium (NaCl-free NGM, hereinafter referred to as cultivation at 0 mM

NaCl). Chemotaxis to high salt after feeding on NGM with a salt concentration of 100 mM NaCl (hereinafter referred to as cultivation at 100 mM NaCl), and chemotaxis after starvation were comparable to those of wild-type animals (Figure 1**b** and Figure 1—figure supplement 1**c**). Neither shortened nor extended cultivation at 0 mM NaCl did not ameliorate the defects (Figure 1—figure supplement 1**d**, **e**), suggesting that the impaired chemotaxis is not due to the delay of behavioral modification. Rather, the mutants are unable to generate migration bias toward low salt. Consistent with this idea, the mutants showed a preference for high salt after cultivation at 50 mM NaCl, under which condition wild-type animals showed unbiased salt preference for either low or high salt concentration (Figure 1**b**). Taken together, JN572 and JN577 show a defect in chemotaxis toward low salt after cultivation in the presence of food.

We mapped mutations of JN572 and JN577 between genetic positions 2.82 and 6.12 (cM) on chromosome II (See Materials and methods, Fay and Bender, 2006; Wicks et al., 2001). Genome sequencing revealed that they carried distinct missense mutations in the *clh-1* gene, one of six ClC channels/transporters in *C. elegans*. Mutations predicted M293I and I146T substitutions in CLH-1A in JN572 and JN577, respectively, and they are hereinafter referred to as *clh-1(pe572)* and *clh-1(pe577)* (Figure 1—figure supplement 2**a**, **b**). Salt chemotaxis defects of the mutants were rescued by a *clh-1(wt)* genomic fragment, confirming that *clh-1* is the responsible gene (Figure 1—figure supplement 2**c**). We also noticed that extra copies of *clh-1(wt)* genomic fragment weakened low-salt chemotaxis of wild type, implying that overexpression of CLH-1 could disrupt chemotaxis to low salt (Figure 1—figure supplement 2**c**).

Interestingly, deletion mutants of *clh-1*, all of which harbor a lesion in the pore-forming transmembrane domain of CLH-1 and hence are putative loss-of-function alleles, showed almost

no discernible defect in salt chemotaxis (Figure 1—figure supplement 2**a**, 3**a**). This result suggests that chemotaxis defects of *clh-1(pe572)* and *clh-1(pe577)* were caused by anomalous activity of *clh-1*. To characterize the nature of *clh-1* missense alleles, we observed food-associated salt chemotaxis of heterozygotes. *clh-1(pe572)/wt* and *clh-1(pe577)/wt* showed normal low-salt chemotaxis, demonstrating that both missense alleles are recessive to wild-type allele (Figure 1**c**). Also, we noted that the effects of both missense alleles on salt chemotaxis are dosage-dependent, that is, *clh-1(pe572)/clh-1(tm1243)* and *clh-1(pe577)/clh-1(tm1243)* showed a modest defect in salt chemotaxis to low salt after cultivation at 0 mM NaCl in contrast to the strong defect of *clh-1(pe572)/clh-1(pe572)* and *clh-1(pe577)/clh-1(pe577)* (Figure 1—figure supplement 3**b**). Furthermore, we unexpectedly found that *clh-1(tm1243)* conferred a weak resistance to an acetylcholine receptor agonist, levamisole. On the contrary, *clh-1(pe572)* or *clh-1(pe577)* caused an enhanced sensitivity to levamisole if compared with wild type, suggesting these alleles may not be simple reduction-of-function alleles (Figure 1—figure supplement 3**c**). Together, these data show that *clh-1(pe572)* and *clh-1(pe577)* (hereinafter collectively referred to as *clh-1(pe)*) are recessive neomorphic mutations whose salt chemotaxis phenotype appears in a dosage-dependent manner.

Given that salt chemotaxis may be affected by the dosage of *clh-1(pe)* alleles, we wondered if overexpression of *clh-1(pe)* can give rise to salt chemotaxis defect. To examine this possibility, we introduced either *clh-1(pe)* genomic DNA fragments into wild type or *clh-1(tm1243)* mutants. Overexpression of mutant *clh-1* conferred defects in low-salt chemotaxis in both genomic backgrounds, demonstrating that excess *clh-1(pe)* override the canonical *clh-1(wt)* function (Figure 1—figure supplement 3**d**). Therefore, excess *clh-1*, either wild-type or *pe*

alleles, can impair low-salt chemotaxis. In conclusion, *clh-1(pe572)* and *clh-1(pe577)* are neomorphic alleles that disrupt chemotaxis to low salt after cultivation at 0 mM NaCl.

ClC proteins redundantly act in salt chemotaxis

All ClC anion channels/transporters characterized so far function as either homodimers or heterodimers (Accardi, 2015; Stölting et al., 2014a). This raised the possibility that mutant CLH-1 molecules impaired the function of other CLH gene products by forming heterodimers with them, thereby resulting in defective salt chemotaxis. To examine this, we observed salt chemotaxis of the mutants whose *clh* genes were deleted individually or in combinations. The *C. elegans* genome carries 6 ClC genes (*clh-1* through *clh-4* for channel, and *clh-5* and *clh-6* for transporter, predicted from a key amino acid residue and subcellular localization, Figure 2—figure supplement 1**a**, Schriever et al., 1999; Nehrke et al., 2000). Each single mutant except for *clh-5(tm6008)* showed normal salt chemotaxis under fed conditions (Figure 2**a**, Figure 2—figure supplement 1**b**). For multiple mutants, we started from *clh-2(ok636) clh-1(tm1243)* double mutants because they had the highest homology (52% identity) among *clh* genes. Although the double mutant showed no chemotaxis defect, triple mutants with either *clh-3(ok763)* or *clh-6(tm617)* showed impaired chemotaxis toward high salt regions, indicating that they act redundantly with *clh-1* and *clh-2* (Figure 2**b**, Figure 2—figure supplement 1**c**). Triple mutants *clh-3(ok763) clh-2(ok636) clh-1(tm1243)* and *clh-5(tm6008) clh-2(ok636) clh-1(tm1243)* showed a weak defect in chemotaxis to low salt. However, the phenotype of *clh-1(pe572)* and *clh-1(pe577)* mutants was not recapitulated in any tested mutants. Interestingly, the defect of *clh-5(tm6008) clh-2(ok636) clh-1(tm1243)* were partially restored in *clh-3(ok763) clh-5(tm6008)*

160 *clh-2(ok636) clh-1(tm1243)* quadruple mutants (Figure 2**b**). These results suggest that the
161 chemotaxis defect of *clh-1(pe)* mutants is unlikely to be due to impairment of other CLH
162 proteins.

163

164 **CLH-1 acts in ASER to affect salt preference after cultivation at 0 mM NaCl**

165 It has previously been reported that *clh-1* is expressed in hypodermal cells, seam cells, D-cells of
166 the vulva, and neuronal and glial cells of the head (Grant et al., 2015; Nehrke et al., 2000). These
167 expression patterns were confirmed with a transcriptional reporter (*clh-1p::nls4::mTFP*, see
168 methods). Of the head neurons, we found that at least ASE, AWA, and AWC sensory neurons
169 expressed the reporter (Figure 3**a**). To determine the site of action of *clh-1*, we performed cell-
170 specific rescue experiments using *clh-1(wt)* cDNA. The mutant phenotype was rescued when
171 cDNA was expressed either pan-neuronally or specifically in ASER, suggesting that *clh-1* acts in
172 the nervous system including ASER (Figure 3**b**, similar results for *pe577*, Figure 3—figure
173 supplement 1**a**). On the other hand, *clh-1(wt)* cDNA failed to rescue *clh-1(pe572)* when
174 expressed either in amphid sheath (AmSh) cells, where CLH-1 function as a pH mediator (Grant
175 et al., 2015), or in the left-sided ASE neuron (ASEL) (Figure 3**b**). Unexpectedly, combined
176 expression of the transgene in ASER and AmSh cells or expression in all ciliated neurons also
177 failed to rescue the phenotype (Figure 3**b**), albeit it recovered chemotaxis of very limited
178 population of animals. These phenotypes are reminiscent of the weakened low-salt chemotaxis
179 by overexpression of *clh-1(wt)* genomic fragment (Figure 1—figure supplement 2**c**), indicating a
180 possibility that excessive function of CLH-1*(wt)* in the tissue near ASER could disturb low-salt
181 chemotaxis.

Morphology of ASER and localization of CLH-1 are largely unaffected by missense mutations

Head sensory neurons of *C. elegans* sense environmental stimuli via neural receptive endings, which are comprised of cilia and microvilli (Perkins et al., 1986; Ward et al., 1975; Ware et al., 1975). Function of these endings largely depends on glia which ensheathe them. A recent study showed that AmSh glia regulate the function and shape of AFD thermosensory neuron's microvilli by modulating efflux of Cl^- to the extracellular space of the receptive endings (Singhvi et al., 2016). In addition, it has been elucidated that CLH-1 transports anions to maintain intracellular pH of AmSh cells (Grant et al., 2015). These results implied the possibility that the receptive ending of ASER may be impaired in *clh-1(pe)* mutants. However, we did not find any notable change in the morphology of ASER including its sensory cilium (Figure 3—figure supplement 1**b**-**d**). Exposure to different salt and food conditions did not affect the length of ASER sensory cilium both in wild type and in *clh-1* mutants, suggesting that the morphology of ASER receptive ending remained largely unchanged (Figure 3—figure supplement 1**e**).

To examine subcellular localization of CLH-1 in ASER, we generated an mTFP-tagged CLH-1 (CLH-1::mTFP). The fusion protein was functional (Figure 3**c**). Fluorescent signals were detected in the plasma membrane and cell organelles (Figure 3**d**, left), as previously reported in mammalian ClC channels and ClC transporters, respectively (Jentsch, 2008, 2007). Localization patterns of CLH-1::mTFP with M293I mutation were comparable to those of wild type (Figure 3**d**, right). These results indicate that the mutation does not affect intracellular localization of CLH-1.

204

205 **Salt stimulus changes intracellular chloride concentration of ASER and this response is**
206 **altered in *clh-1(pe)* mutants**

207 Previous studies showed that CLH-1 mediates flux of univalent anions including chloride and
208 bicarbonate. Furthermore, electrophysiological characterization of CLH-1 using *Xenopus* oocytes
209 indicated that CLH-1 is an inwardly rectifying channel that conduct Cl^- (Grant et al., 2015;
210 Nehrke et al., 2000). Our genetic analyses suggested the *clh-1(pe)* mutations might be
211 neomorphic. To examine whether the mutations affected the property of CLH-1 conductance, we
212 expressed mutant CLH-1 in *Xenopus* oocytes and measured membrane currents via two-
213 electrode voltage clamping. Wild-type CLH-1 showed inwardly rectifying currents from -160 to
214 -80 mV as previously reported (Figure 4**a-e**, Grant et al., 2015; Nehrke et al., 2000). Similar
215 currents were also observed in both CLH-1(M293I) and CLH-1(I146T). This result supports the
216 idea that the basic function of CLH-1 as a voltage-dependent anion channel is retained in CLH-
217 1(M293I) and CLH-1(I146T) mutants.

218 Next, we asked how *clh-1* mutations disturb salt chemotaxis of *C. elegans*. We focused
219 on the salt-sensing neuron ASER, one of the site-of-action of *clh-1*, and which is essential for
220 food-associated salt concentration chemotaxis (Kunitomo et al., 2013). ASER is activated by salt
221 concentration decreases and deactivated by salt concentration increases (Suzuki et al., 2008, see
222 below). Given that CLH-1 localized to the membranous compartments of ASER (Figure 3**d**) and
223 acted as a chloride channel (Figure 4**a-e**), we hypothesized that CLH-1 might be involved in
224 chloride dynamics during salt response of ASER. To examine this possibility, we monitored
225 intracellular chloride ($[Cl^-]_i$) dynamics of ASER by utilizing the genetically encoded chloride

indicator, Superclomeleon. This probe is a FRET-type indicator in which the YFP/CFP fluorescence ratio decreases upon binding to chloride ions (Grimley et al., 2013). Animals were cultivated at 0 mM NaCl with food and immobilized in the olfactory chip (Chronis et al., 2007), and a NaCl down-step from 50 mM to 25 mM was applied as salt stimulus. In wild type, YFP/CFP ratio decreased upon salt down-step, indicating that $[Cl^-]_i$ of ASER was increased when the neuron was activated (Figure 4**f**). This response is not, at least solely, mediated by CLH-1 because it was also observed in *clh-1(tm1243)* mutants. Notably, the magnitude of YFP/CFP ratio change was significantly larger in *clh-1(pe)* mutants, suggesting that ASER $[Cl^-]_i$ greatly increased in mutants (Figure 4**g**).

ASER salt response is altered in *clh-1* mutants

Intracellular chloride concentration increase can antagonize depolarization of neurons. We then wanted to look into whether *clh-1* mutations affect the activity of ASER in response to salt stimulus. As aforementioned, ASER is activated by salt concentration decreases, which is indicated by an increase in intracellular calcium levels, whereas it is deactivated by salt concentration increases (Suzuki et al., 2008). Such ASER responsivity is basically retained regardless of cultivation salt concentrations or food availability (Kunitomo et al., 2013; Oda et al., 2011).

We performed *in vivo* calcium imaging in wild type and *clh-1* mutants using a genetically encoded calcium indicator YC2.6 (Chronis et al., 2007; Horikawa et al., 2010). Animals were cultivated at either 0 mM NaCl or 100 mM NaCl with or without food, and ASER was stimulated by repeated salt concentration changes from 50 mM NaCl to 25 mM NaCl, to

observe responses to both down-step and up-step stimuli. After cultivation at 0 mM NaCl, the amplitude of calcium response to the first down-step stimulus was comparable between wild type and *clh-1* mutants. However, the response to the second down-step was diminished in *clh-1(pe)* mutants compared to wild type (Figure 5**a**, **b**). A similar trend was observed in the third down-step response. The decay of intracellular calcium level ($[Ca^{2+}]_i$) was small in the *clh-1(pe)* mutants, which was more evident after salt up-step (Figure 5—figure supplement 1**a**, **b**). This diminished decay was likely responsible for the decreased calcium response to the repeated stimuli. On the other hand, ASER salt response of *clh-1(tm1243)* was similar to that of wild type, except that the decay was significantly large during the first down-step stimulus (Figure 5**a**, **b** and Figure 5—figure supplement 1**a**, **b**). Interestingly, reduction of ASER response amplitude upon repeated salt down-step stimuli was not obvious after cultivation at 100 mM NaCl with food, although *clh-1(pe572)* constantly showed small ASER responses (Figure 5**c**, **d** and Figure 5—figure supplement 1**c**, **d**). Considering the essential role of ASER in salt concentration chemotaxis, these results imply that hampered chemotaxis of *clh-1(pe)* mutants toward low salt after low-salt cultivation is probably due to the abnormal ASER responsivity to salt concentration change.

Consistent with previous reports, salt responses of ASER of starved wild-type animals were not largely different when compared to that of fed animals. However, the ASER activity patterns of *clh-1* mutants starved at 0 mM were distinct from those of fed animals (please compare Figure 5, Figure 5—figure supplement 1 and Figure 5—figure supplement 2). After cultivation at 0 mM without food, for example, the amplitude of activation of *clh-1(pe577)* mutants were even larger than that of wild type (Figure 5—figure supplement 2**a-c**). Meanwhile, the difference of ASER salt responses between wild type and *clh-1(pe)* mutants were less

obvious after starvation at 100 mM NaCl (Figure 5—figure supplement 2**e-h**). Taking all these into account, we concluded that mutations in *clh-1* affect responsivity of ASER, most notably in the reduced response to repeated salt down-step and up-step stimuli after cultivation at 0 mM NaCl with food.

Behavioral strategies for chemotaxis are disrupted in *clh-1(pe)* mutants

Next, we quantitatively analyzed the navigation behavior of *clh-1* mutants to examine which behavioral components are affected. *C. elegans* utilize at least two behavioral strategies to achieve salt chemotaxis: klinokinesis and klinotaxis. In klinokinesis, migration bias is generated by controlling the frequency of steep turns called pirouettes, which are typically accompanied by reversals and omega turns. The bout of pirouette is triggered according to cumulative salt concentration change along an animal's progression (Pierce-Shimomura et al., 2001). In klinotaxis, animals gradually curve towards their preferred direction by sensing fluctuation of salt concentration accompanying head bending (Iino and Yoshida, 2009). Input to ASER is both required and sufficient for fed animals to generate the two behavioral strategies (Kunitomo et al., 2013; Satoh et al., 2014). We found that klinotaxis bias was severely impaired in *clh-1(pe)* mutants regardless of cultivation salt concentrations (Figure 6**a**, Figure 6—figure supplement 1**a** and **c**). Klinokinesis bias of the *clh-1(pe)* animals after cultivation at 100 mM NaCl was comparable to that of wild type (Figure 6**b**, Figure 6—figure supplement 1**d**). These results suggest that chemotaxis of *clh-1(pe)* animals to high salt after cultivation at 100 mM NaCl largely depends on klinokinesis. However, after cultivation at 0 mM NaCl, klinokinesis bias was lost in *clh-1(pe)* mutants. Up-regulation of pirouette frequency along with salt concentration

293 increase (dC/dt > 0) was abolished in *clh-1(pe)* mutant animals (Figure 6**b** and Figure 6—figure
294 supplement 1**b**). These results strongly indicate that the defective chemotaxis of *clh-1(pe)*
295 mutants is due to loss of both klinotaxis and klinokinesis biases after cultivation at 0 mM NaCl.
296 The klinokinesis and klinotaxis of *clh-1(tm1243)* mutants were comparable to those of wild type
297 (Figure 6**a**, **b** and Figure 6—figure supplement 1**a**, **b**).

298

299 **Reduced salt response of AIB to salt increase in *clh-1(pe572)* mutants**

300 Quantitative analysis of chemotaxis revealed that klinokinesis was disrupted in *clh-1(pe572)* and
301 *clh-1(pe577)* mutants upon increase in salt concentration (Figure 6**b**, Figure 6—figure
302 supplement 1**b**). To further gain insight into the neural mechanism of this phenomenon, we
303 focused on AIB, a postsynaptic interneuron of ASER which promotes sensory stimulus-
304 dependent reversals, the trigger of pirouettes (Piggott et al., 2011; Zou et al., 2018). Because the
305 synapse between ASE and AIB is proposed as the site of plasticity that regulate klinokinesis bias
306 in salt chemotaxis (Kunitomo et al., 2013; Luo et al., 2014; Wang et al., 2017), we hypothesized
307 that the responsivity of AIB may be altered in these mutants. To examine this possibility, we
308 observed salt responses of AIB in freely behaving animals using a microfluidics arena (Albrecht
309 and Bargmann, 2011). Animals were cultivated at 0 mM NaCl with food and stimulated by an
310 up-step NaCl stimulus from 0 mM to 25 mM. Wild-type animals responded to the salt stimulus
311 by slowing down or reversal (the moving velocity becomes less than zero, Figure 6**c** and Figure
312 6—figure supplement 2). *clh-1(pe572)* mutants also showed reduction in speed, but the
313 proportion of animals that exhibited reversal was relatively smaller than wild type (see legend for
314 detailed criterion of reversal, Figure 6**d**). These results agreed with the klinokinesis defect

observed on chemotaxis plates (Figure 6**b** and Figure 6—figure supplement 1**b**). Importantly, responses of AIB to salt up-step correlated well with behaviors. AIB was largely activated upon salt stimulus in wild type, whereas less activated in *clh-1(pe572)* (Figure 6**e**, **f**). Collectively, our results indicate that salt signal mediated by AIB is diminished in *clh-1(pe572)* mutants, and resulted in reduction of turning frequency upon salt up-step after cultivation at 0 mM NaCl.

Discussion

Here, using genetic, molecular, neurophysiological and behavioral analyses, we showed that the ClC chloride channel CLH-1 is involved in migration bias on salt gradient after feeding. This is probably conducted by, i) maintaining ASER responsivity to repeated salt stimuli that affect klinotaxis, and ii) participating in salt up-step response of ASER and thereby of AIB after cultivation at low salt that contribute to klinokinesis (Figure 7). Repeated activation of ASER synchronized with head swing generates biased klinotaxis (Satoh et al., 2014). Calcium imaging of ASER showed reduced responsivity to repeated down-steps in *clh-1(pe)* mutants (Figure 5**a**-**b** and Figure 5—figure supplement 1**a**). This result implies that temporal resolution of ASER is impaired in the mutants. Behavior analysis revealed that klinotaxis was actually disrupted regardless of previous cultivation conditions (Figure 6**a** and Figure 6—figure supplement 1**a**, **c**). Our data is consistent with the idea that dynamic $[Ca^{2+}]_i$ fluctuation in ASER that reflects environmental NaCl concentration change is required for generation of klinotaxis. In addition, *clh-1(pe)* mutants showed klinokinesis defect upon salt increase after cultivation at 0 mM NaCl (Figure 6**b** and Figure 6—figure supplement 1**b**). In agreement with this, ASER response to salt up-step, that is, the R/R_0 decay2 of $[Ca^{2+}]_i$, were reduced in *clh-1(pe)* mutants (Figure 5**a** and

Figure 5—figure supplement 1**b**). Furthermore, the response of AIB and reversal behavior upon salt up-step were reduced in *clh-1(pe572)* animals (Figure 6**d**, **f**). Suppression of AIB activity results in reduction of turning frequency (Gordus et al., 2015; Piggott et al., 2011), which is consistent with the idea that inability of AIB to properly respond salt increase gave rise to reduced migration toward low salt regions.

Our results showed that chloride influx into ASER, which was evoked by salt decrease after cultivation at 0 mM, was larger in *clh-1(pe)* mutants compared to wild type (Figure 4**f**, **g**). In general, influx of anion produces outward currents that cause hyperpolarization or prevent depolarization in neurons (Staley et al., 1995). There are several possible mechanisms that could explain increased chloride influx by *clh-1(pe)* mutations (Figure 7, middle). One is a difference in ASER's transmembrane chloride potential between genotypes. ClC proteins, as well as other chloride transporters such as KCCs and NKCCs, are involved in the excitability of neurons through their homeostatic roles in regulating cellular ionic milieu (Jentsch, 2008; Stauber et al., 2012). Another possible mechanism is elevated anion intrusion via CLH-1*(pe)* channels. ClC-2, the closest mammalian homolog of CLH-1, was shown to be involved in chloride influx into neuronal cells, probably due to incomplete rectification (Ratté and Prescott, 2011; Rinke et al., 2010). In *C. elegans*, CLH-3 inhibit excitability of HSN neurons, which control egg-laying behavior, by directly mediating chloride influx (Branicky et al., 2014). Furthermore, Grant et al. has suggested a possibility that CLH-1 contributes to anion influx with regard to pH maintenance in AmSh (Grant et al., 2015). Since chloride traffic across membranes can affect electrochemical potential of other ions, the altered $[Cl^-]_i$ dynamics might affect cellular $[Ca^{2+}]_i$ dynamics and excitability. ClC-1, another close mammalian homolog of CLH-1 (37% identity), is involved in excitability of muscle fibers by controlling chloride transportation. Mutations of ClC-1, which

are generally attributed to reduction of channel functions, have been identified to cause incomplete repolarization after action potentials, resulting in prolonged electrical activity and muscle stiffness (Adrian and Bryant, 1974; Fahlke et al., 1995; Pusch et al., 1995; Rhodes et al., 1999; Stölting et al., 2014b; Wu, 2002). These reports lend support to the idea that increased chloride influx affect $[Ca^{2+}]_i$ dynamics of ASER and thereby reduce responsivity of the cell to salt stimuli. These scenarios, together with further characterization of channel properties of CLH-1, needs to be demonstrated in the future study.

In the levamisole resistance test, missense (*pe572* and *pe577*) and the deletion (*tm1243*) allele of *clh-1* showed an opposite phenotype (Figure 1—figure supplement 3**c**). In addition, overexpression of *clh-1(wt)* impaired low-salt chemotaxis; the effect was enhanced in the case of *clh-1(pe)* alleles (Figure 1—figure supplement 2**c** and 3**d**). These results suggest that the *clh-1(pe)* mutations are neomorphic or perhaps hypermorphic alleles. ClC proteins act in homo- or heterodimers (Stölting et al., 2014a). It is not predictable whether CLH-1*(pe)*/CLH-1*(wt)* heterodimer shows mutant-type or wild-type activity. The recessiveness of *clh-1(pe)* mutations (Figure 1**c**) can be explained by assuming that the heterodimer shows wild-type activity.

ASER makes synapses to three first layer interneurons, AIA, AIB and AIY. Activation of AIA and AIY are known to promote forward locomotion, while activation of AIB promotes reversals (Gray et al., 2005; Piggott et al., 2011; Zou et al., 2018). Also, salt response of AIB is markedly changed by salt experience. AIB is activated by salt concentration decrease if previously-experienced salt concentrations were high, whereas it is rather deactivated after cultivation at low salt (Kunitomo et al., 2013; Luo et al., 2014). Here we showed that AIB can be activated by salt increase after cultivation at low salt, which was reduced in *clh-1(pe572)* mutant

(Figure 6**e**, **f**). Considering that ASER is glutamatergic (Serrano-Saiz et al., 2013), there may be both excitatory and inhibitory transmission between ASER and AIB. Indeed, AIB expresses the AMPA-type glutamate receptor GLR-1, which mediates excitatory glutamatergic inputs from sensory neurons (Chalasani et al., 2007; Zou et al., 2018). Besides, it has recently been suggested that the glutamate-gated chloride channel GLC-3 and AVR-14 may mediate inhibitory inputs to AIB (Kuramochi and Doi, 2019; Summers et al., 2015). These observations raise the possibility that glutamate response of AIB depends on the electrochemical gradient of Cl^- across the membrane as well as the balance of excitatory and inhibitory receptors. In other words, under the condition in which inhibitory glutamate receptors were dominant, AIB could be disinhibited by reduction of presynaptic glutamate release. Growing evidence highlights the importance of chloride homeostasis in the function of the nervous system. In mammalian hippocampal neurons, intracellular chloride is elevated during embryonic development and thereby renders GABAergic transmission excitatory, which is necessary for maturation of synaptic network (Pfeffer et al., 2009). Furthermore, chloride transportation through NKCC1 regulates synaptic plasticity and memory formation in adult hippocampal neurons (Deidda et al., 2015). It will be of interest in the future to determine how the extracellular ionic milieu and glutamate receptors orchestrate the responsiveness of AIB.

In this study we showed that ClC chloride channels function redundantly in salt chemotaxis of *C. elegans*. Food-associated salt chemotaxis was normal in each single (*clh-1(tm1243) II*, *clh-2(ok636) II*, *clh-3(ok763) II*, or *clh-4(ok1162) X*) or double (*clh-2(ok636) clh-1(tm1243) II*) mutants of ClC chloride channel genes (Figure 2**a**, **b**). However, the triple (*clh-3(ok763) clh-2(ok636) clh-1(tm1243) II*) mutation had a marked effect on behavior (Figure 2**b**). Interestingly, all three genes are located very closely on chromosome II (4.08 +/- 0.003 cM for

405 *clh-1*, 3.46 +/- 0.003 cM for *clh-2*, 0.50 +/- 0.000 cM for *clh-3*), suggesting that they are derived
406 by duplication and they might share some evolutionarily conserved functions. The CLH-5
407 putative anion transporter is also located close to the aforementioned ClC channels on
408 chromosome II: 1.01 +/- 0.007 cM. In addition, mutation of *clh-6(tm617) V*, which encodes a
409 putative anion transporter and whose single mutation had no effect on salt chemotaxis, also gave
410 rise to salt chemotaxis defect in combination with *clh-2(ok636) clh-1(tm1243) II* mutations. Only
411 a few studies so far have addressed functional redundancy of ClC family proteins in an organism
412 (Jeworutzki et al., 2014; Stölting et al., 2014a), and our study provides an insight into functional
413 differences and redundancies of ClC family proteins.

Figure 1

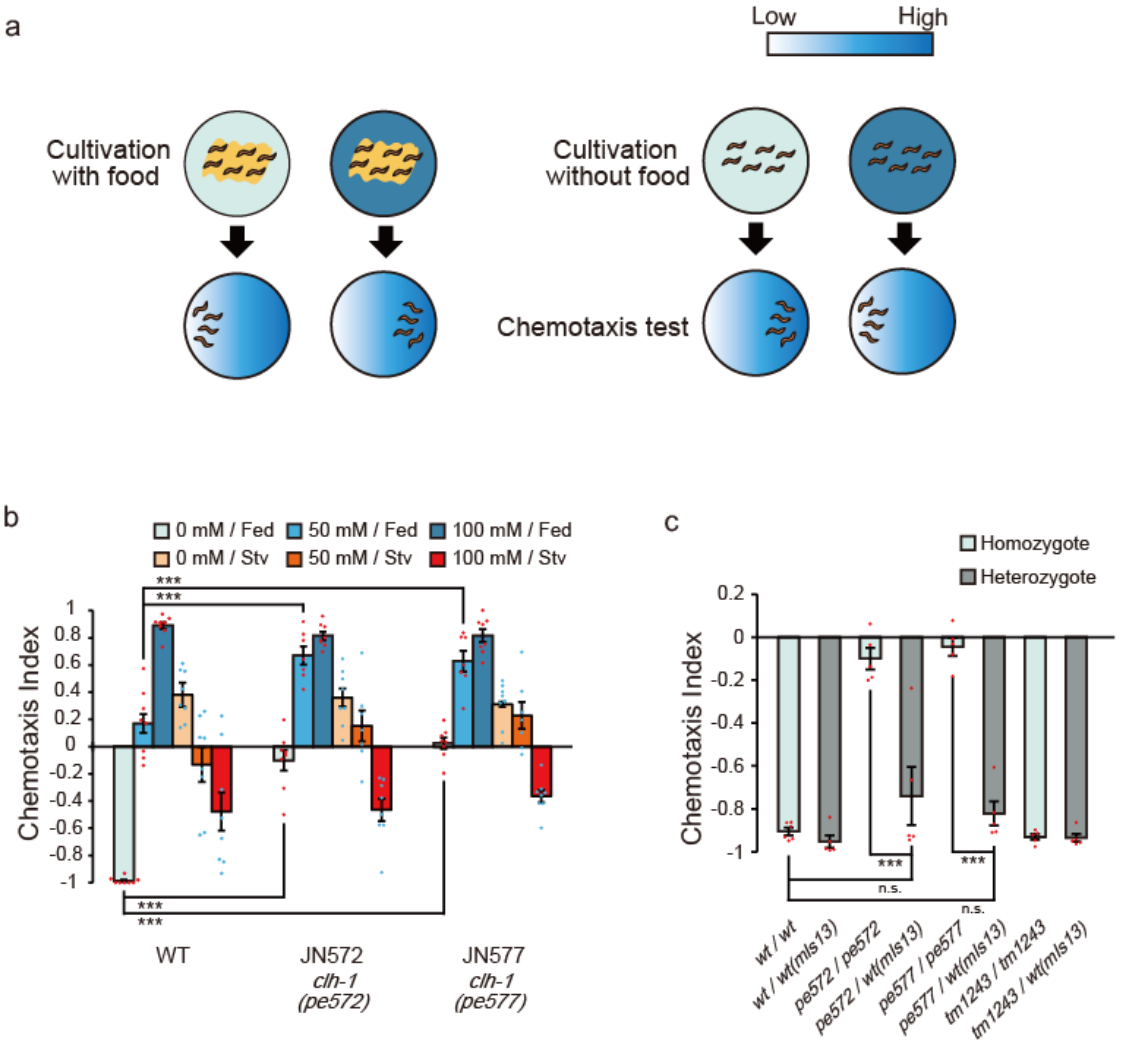

Figure 1 with 3 supplements

Two missense mutations in *clh-1* give rise to food-associated salt chemotaxis disorder

(**a**) Salt concentration chemotaxis. Animals were cultivated at 0 mM or 100 mM of NaCl with or without food and placed on an assay plate with NaCl gradient. Distribution of animals was quantified by calculating a chemotaxis index. See method for details. (**b**) Chemotaxis of wild-type animals and two mutants obtained from screening, JN572: *clh-1(pe572)* and JN577: *clh-1(pe577)*. Dots show the result of individual trials. Bar and the error bar represent mean +/- s.e.m., $n = 8$ assays, Dunnett's test, $***p < 0.001$, n.s., not significant. (**c**) Chemotaxis of *clh-1* heterozygotes. *clh-1* homozygotes were crossed with a *clh-1(wt)* reporter strain that express GFP in pharyngeal muscle (*mIs13*). Resulted F1 animals were used for assay. Dots show the result of individual trials. Bar and the error bar represent mean +/- s.e.m., $n \geqq 4$, Tukey's test, $***p < 0.001$.

Figure 1—figure supplement 1

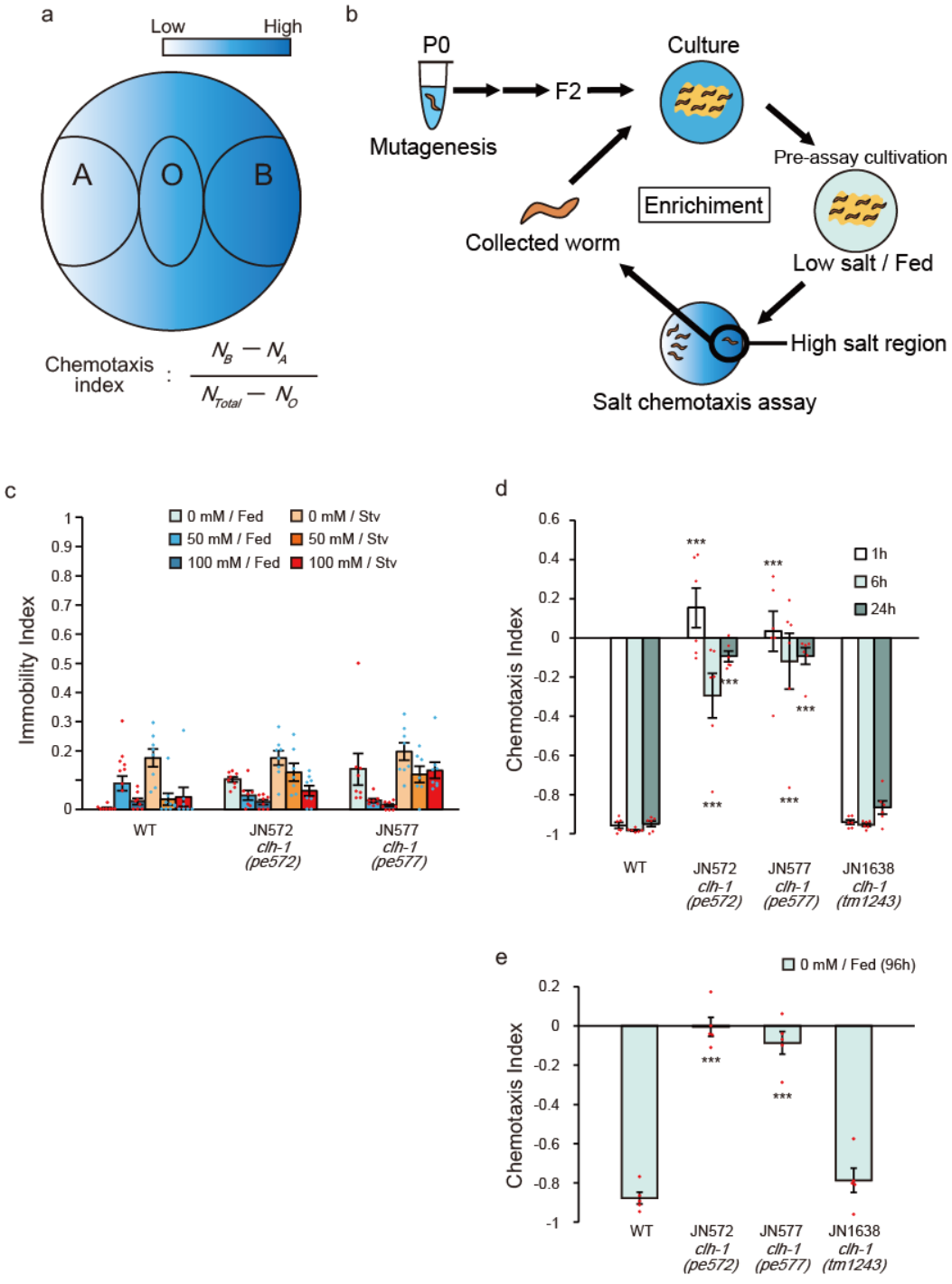

428

Figure 1—figure supplement 1

Isolation and characterization of salt chemotaxis mutants JN572 and JN577

(**a**) A schematic diagram of salt chemotaxis assay plate. See methods for details. (**b**) Procedure for forward genetic screening to obtain food-associated salt chemotaxis mutants. Wild-type animals were mutagenized with ethyl methanesulfonate (EMS), and F2 animals were applied for salt chemotaxis assay. Animals that showed defective chemotaxis were isolated and propagated for another round of test to enrich the ratio of mutants. (**c**) Immobility of wild type, JN572 and JN577. See method for details. Dot shows the result of individual trials. Bar and the error bar represent mean +/- s.e.m., $n = 8$ assays. (**d** and **e**) Chemotaxis of wild type and *clh-1* mutants after different duration of pre-assay cultivation. Animals were fed at 0 mM NaCl for 1, 6 or 24 hours (**d**) or 96 hours (from birth until just prior to assay, **e**) and tested for salt chemotaxis assay. Dot shows the result of individual trials. Bar and the error bar represent mean +/- s.e.m., $n \geqq 6$, compared with wild type, Dunnett's test, $***p < 0.001$.

Figure 1—figure supplement 2

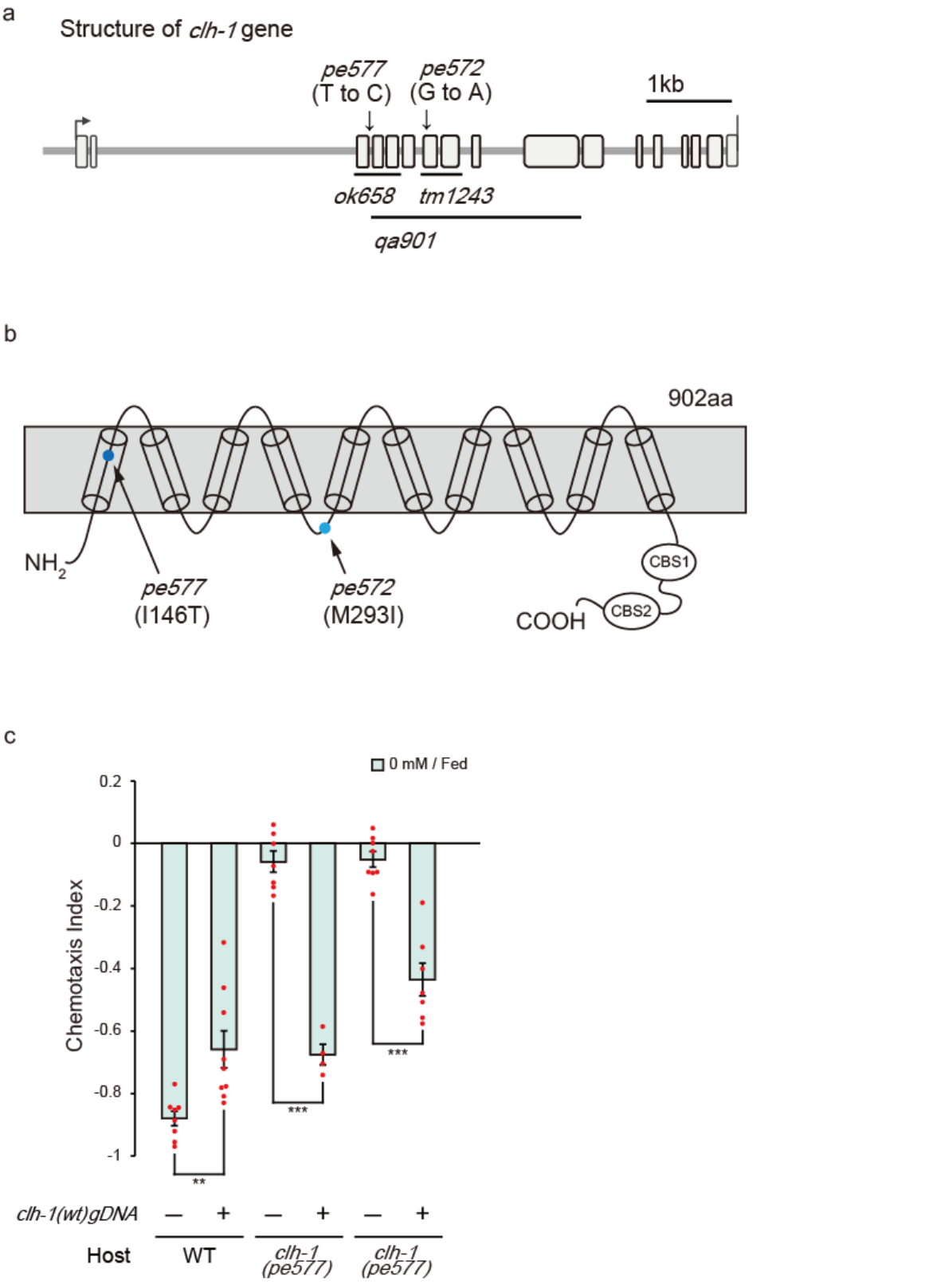

444 **Figure 1—figure supplement 2**

445 Missense mutations in *clh-1* are responsible for salt chemotaxis defect

446 (**a**) Gene structure of *clh-1* and the positions of *clh-1* mutations. The positions of *pe572* (T to C)
447 and *pe577* (G to A) are noted by arrows. *ok658* removes exon 3 to 5, *tm1243* removes exon 6
448 and 7, *qa901* removes exon 4 to 10. (**b**) Predicted protein structure of CLH-1. The positions of
449 *pe572* (I146T) and *pe577* (M293I) are noted by arrows. CBS1 and CBS2 indicate cystathionine
450 beta synthase domains, which are known as protein binding domains. (**c**) Rescue of *clh-1(pe572)*
451 and *clh-1(pe577)* mutants by a *clh-1* genomic DNA fragment. Dot shows the result of individual
452 trials. Bar and the error bar represent mean +/- s.e.m., $n \geqq 4$ assays, Tukey's test, $***p < 0.0001$,
453 $**p < 0.01$.

Figure 1—figure supplement 3

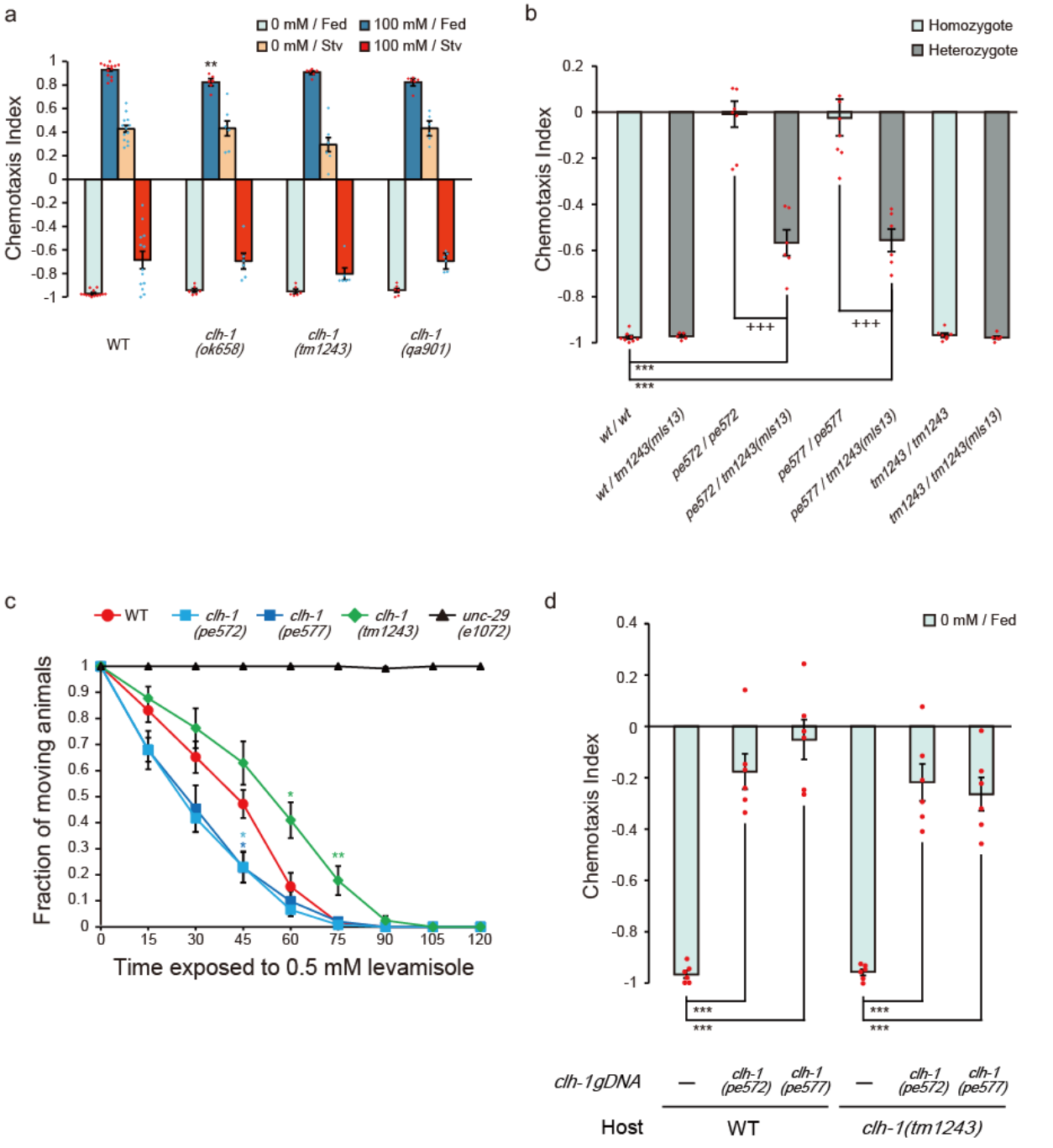

455 **Figure 1—figure supplement 3**

456 Characterization of *clh-1* mutants

457 (**a**) Chemotaxis of *clh-1* deletion mutants. Dot shows the result of individual trials. Bar and the
458 error bar represent mean +/- s.e.m., $n \geqq 6$ assays, compared with wild type, Dunnett's test, $^{**}p <$
459 0.01. (**b**) *pe572* and *pe577* show haploinsufficiency. For generating heterozygotes,
460 hermaphrodites of either wild type, *clh-1(pe572), clh-1(pe577)* or *clh-1(tm1243)* were crossed
461 with *clh-1(tm1243)* males which express GFP in pharyngeal muscle (*mIs13*), and F1 animals
462 were used for the assay. Dot shows the result of individual trials. Bar and the error bar represent
463 mean +/- s.e.m., $n \geqq 5$ assays, Tukey's test, $^{***}p < 0.001$, compared with wild-type
464 homozygote. $+++p < 0.001$, compared with each original missense allele homozygote. (**c**)
465 Levamisole resistance test. Graph shows fraction of non-paralyzed (moving) animals at indicated
466 time after placed on 0.5 mM levamisole. Mean +/- s.e.m., $n = 6$ assays, compared with wild
467 type, Dunnett's test, $^{**}p < 0.01$, $^{*}p < 0.05$. Asterisks are colored according to the strain (light
468 blue* for *clh-1(pe572)*, deep blue* for *clh-1(pe577)*, green* for *clh-1(tm1243)* (**d**) Excess
469 genomic DNA fragments of *clh-1(pe572)* or *clh-1(pe577)* recapitulate salt chemotaxis defect in
470 wild type and *clh-1(tm1243)*. Dot shows the result of individual trials. Bar and the error bar
471 represent mean +/- s.e.m., $n = 6$ assays, Tukey's test, $^{***}p < 0.001$.

Figure 2

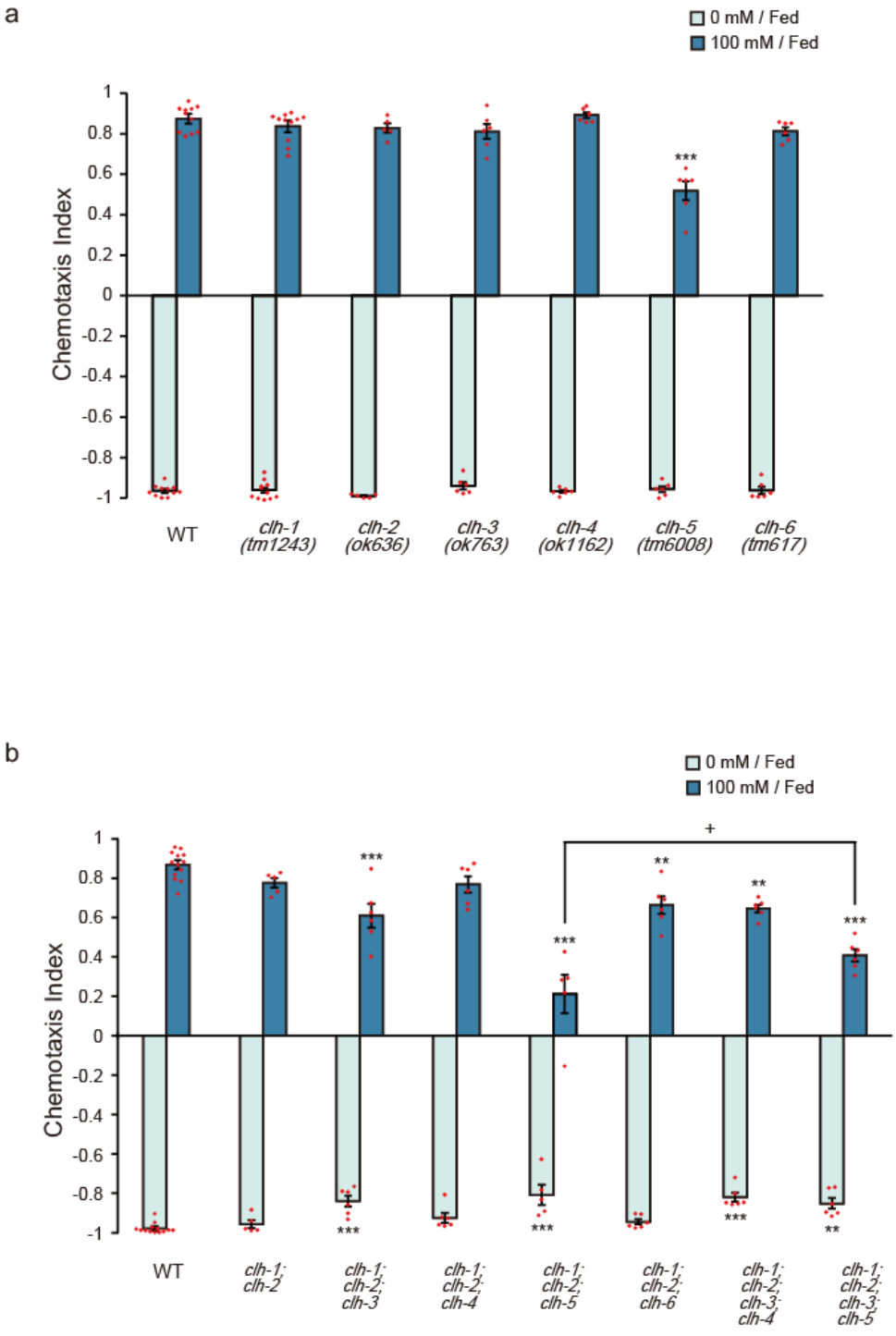

Figure 2 with 1 supplement

ClC genes function redundantly in salt chemotaxis

(**a**) Chemotaxis of deletion mutants of 6 ClC genes (*clh-1* to *clh-6*). All mutant strains were outcrossed with wild type more than 4 times. Dot shows the result of individual trials. Bar and the error bar represent mean +/- s.e.m., $n \geqq 5$ assays, compared with wild type, Dunnett's test, $***p < 0.001$. (**b**) Chemotaxis of *clh* multiple mutants. Dot shows the result of individual trials. Bar and the error bar represent mean +/- s.e.m., $n \geqq 5$ assays, Tukey's test, $***p < 0.001$, $**p < 0.01$, $*p < 0.05$, compared with wild type. $+p < 0.05$, compared between indicated mutants.

Figure 2—figure supplement 1

a

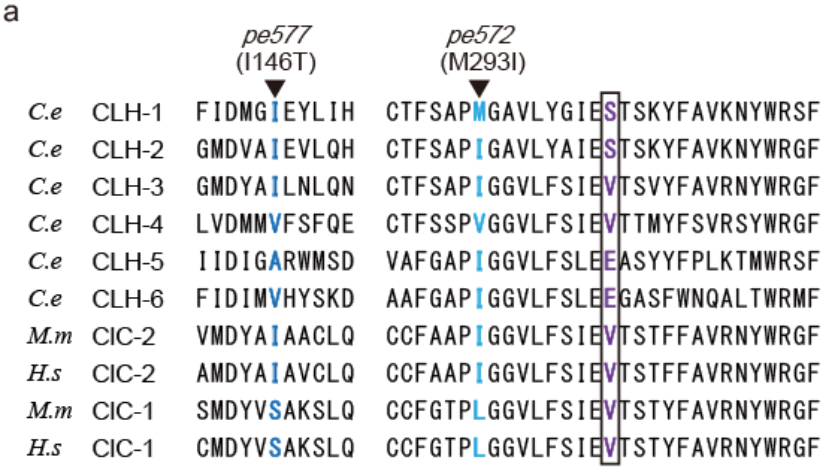

b

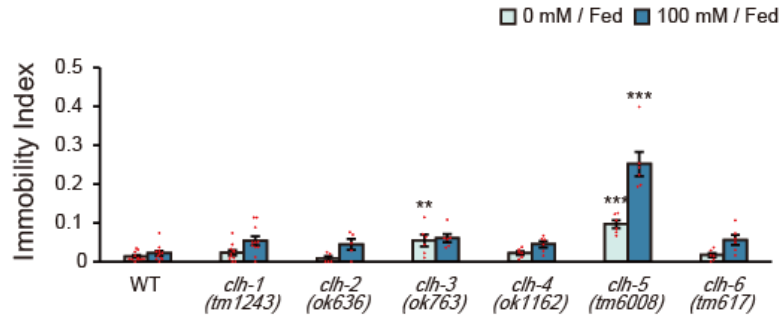

c

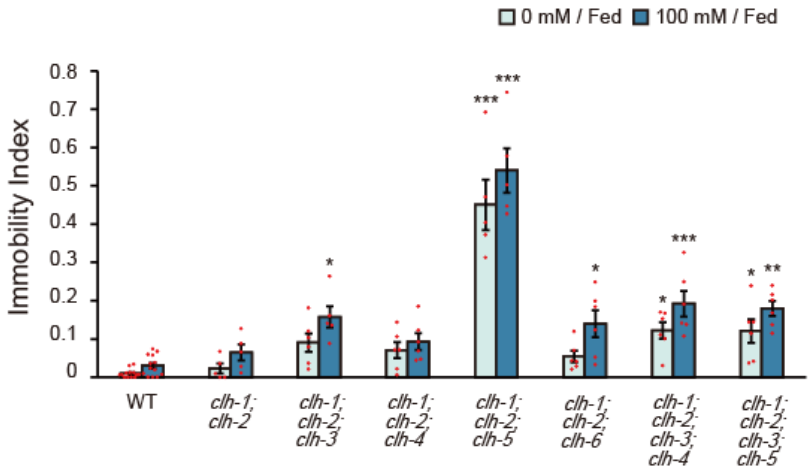

481

Figure 2—figure supplement 1

Characteristics of *C. elegans* ClC anion channels and transporters

(**a**) Comparison of *C. elegans* (*C.e*) CLHs, murine (*M.m*) and human (*H.s*) ClC-2 and ClC-1. Amino acids altered in *clh-1(pe)* alleles (deep and light blue) and flanking regions are shown. The "Gating glutamate" residue is boxed, which predicts whether the corresponding ClC protein is an anion channel or a H^+/Cl^- antiporter (Dutzler et al., 2002). Members that carry glutamate (E) at the position is proposed as a H^+/Cl^- antiporter, whereas anion channel if it is valine (V). Although CLH-1 and CLH-2 carry serine (S) residue at this position, they are presumed to be anion channels because they share high similarity with mammalian ClC-2 (Schriever et al., 1999; Nehrke et al., 2000). (**b**) Immobility of *clh* deletion mutants (*clh-1* to *clh-6*). Dot shows the result of individual trials. Bar and the error bar represent mean +/- s.e.m., $n \geqq 5$ assays, compared with wild type, Dunnett's test, $***p < 0.001$, $**p < 0.01$. (**c**) Immobility of *clh* multiple mutants. Dot shows the result of individual trials. Bar and the error bar represent mean +/- s.e.m., $n \geqq 5$ assays, Tukey's test, $***p < 0.001$, $**p < 0.01$, $*p < 0.05$, compared with wild type.

Figure 3

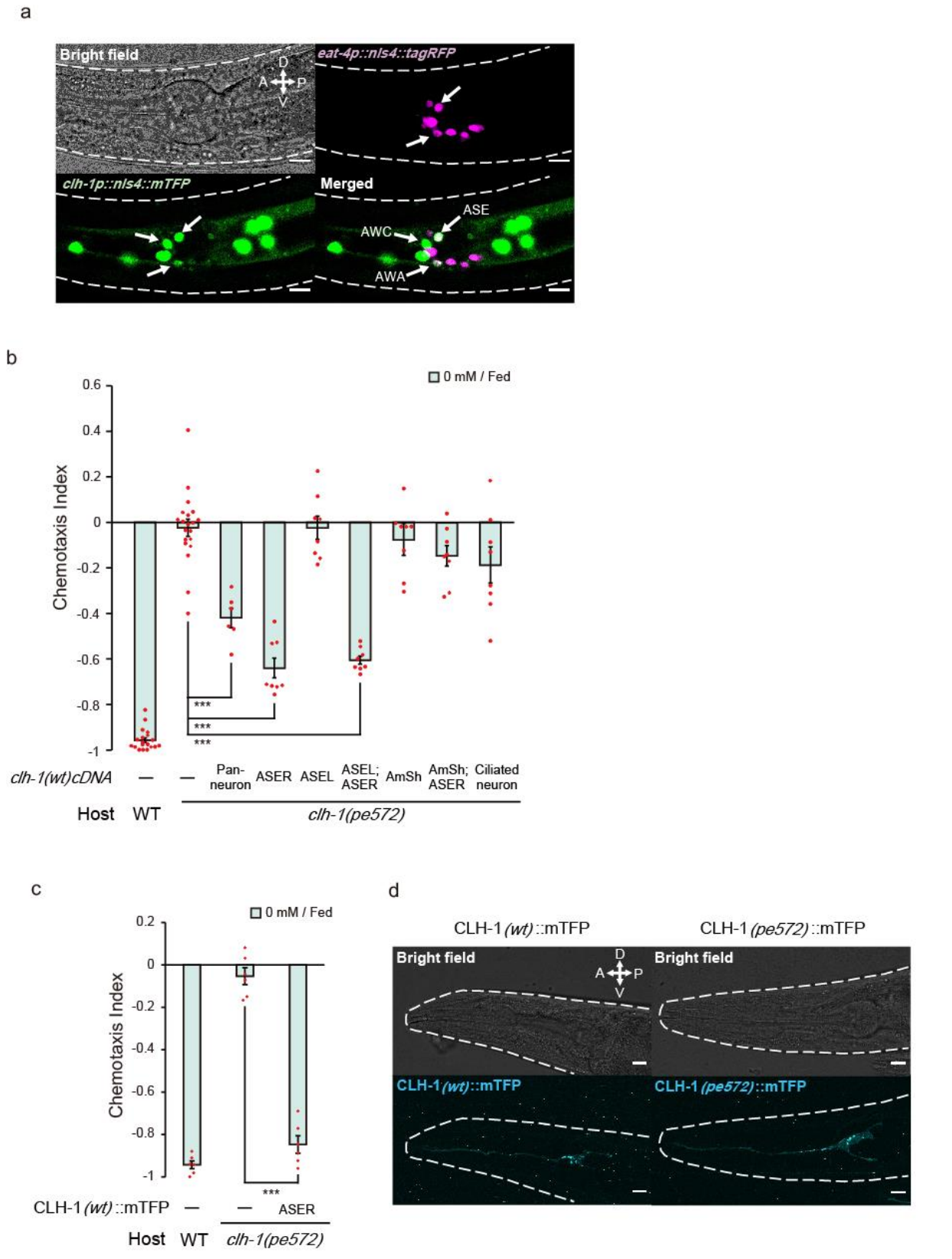

497

Figure 3 with 1 supplement

clh-1 acts in the salt sensing neuron ASER

(**a**) Expression pattern of *clh-1p::nls4::mTFP* (green) in an adult animal that express glutamatergic neuron-specific marker *eat-4p::nls4::tagRFP* (magenta). Three pairs of sensory neurons, namely, AWA, AWC and ASE expressed *clh-1p::nls4::mTFP*. DiI, which stain 6 pairs of head sensory neurons, was also used as a position marker for cell identification (data not shown). Scale bar = 10 µm. (**b**) Rescue of *clh-1(pe572)* mutants by cell-specific expression of *clh-1(wt)* cDNA. Promoters used in this experiment are as follows; *rimb-1p* for all neurons, *gcy-5p* for ASER, *gcy-7p* for ASEL, *vap-1p* for amphid sheath cells, *dyf-11p* for ciliated neurons. Dot shows the result of individual trials. Bar and the error bar represent mean +/- s.e.m., $n \geqq 6$ assays, Tukey's test. ***$p < 0.001$. (**c**) Chemotaxis of *clh-1(pe572)* mutants that express *clh-1(wt)cDNA::mTFP* in ASER. mTFP-tagged CLH-1 is functional. Dot shows the result of individual trials. Bar and the error bar represent mean +/- s.e.m., $n = 6$ assays, Tukey's test. ***$p < 0.001$. (**d**) Expression of *gcy-5p::clh-1(wt)cDNA::mTFP* in wild type (left) and *gcy-5p::clh-1(pe572)cDNA::mTFP* in *clh-1(pe572)*. Both CLH-1*(wt)*::mTFP and CLH-1*(pe572)*::mTFP fluorescence were observed in membrane of dendrite, soma, axon and cell organelles. Scale bar = 10 µm.

Figure 3—figure supplement 1

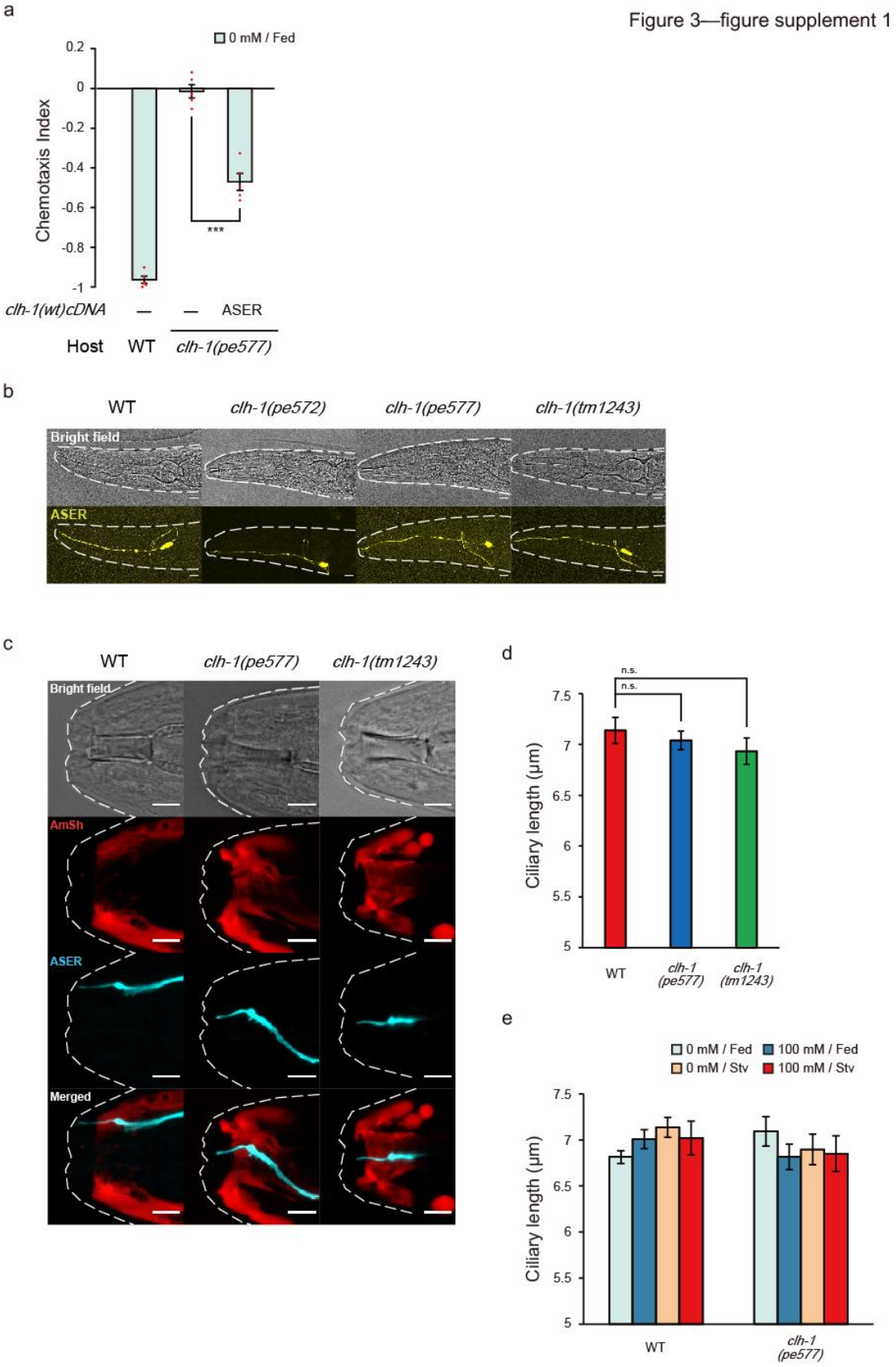

516 **Figure 3—figure supplement 1**

517 *clh-1* acts in ASER but mutations in *clh-1* do not affect gross morphology of ASER

518 (**a**) Rescue of *clh-1(pe577)* mutants by ASER-specific expression of *clh-1(wt)* cDNA. The
519 cDNA was expressed in ASER by *gcy-5* promoter. Dot shows the result of individual trials. Bar
520 and the error bar represent mean +/- s.e.m., $n = 5$ assays, Tukey's test. ***$p < 0.001$. (**b**)
521 Morphology of ASER in wild-type and *clh-1* adult animals visualized by *gcy-5p::GFP*. No gross
522 defect was observed in the mutants. Animals were anesthetized by 10 mM NaN_3. Bright field
523 (top) and stacked confocal fluorescence images (bottom). Scale bar = 10 μm. (**c**) Confocal
524 images of ASER sensory cilium and amphid sheath glial cells in adult animals. Top; bright field,
525 second top; AmSh (*vap-1p::mCherry*, red), second bottom; ASER *(gcy-5p::mTFP*, cyan*)*,
526 bottom; merged. Animals were anesthetized by 100 mM levamisole. Scale bar = 5 μm. (**d**)
527 Length of ASER sensory cilium in adult animals. Animals were anesthetized by 100 μM
528 levamisole and ciliary length was measured from confocal images. Mean +/- s.e.m., $n \geqq 16$
529 animals, Dunnett's test. (**e**) Length of ASER sensory cilium in adult animals after cultivation at
530 the indicated condition. Animals were anesthetized by 100 μM levamisole. Ciliary length was
531 measured from confocal images. Mean +/- s.e.m., $n \geqq 8$ animals, Tukey's test.
532

Figure 4

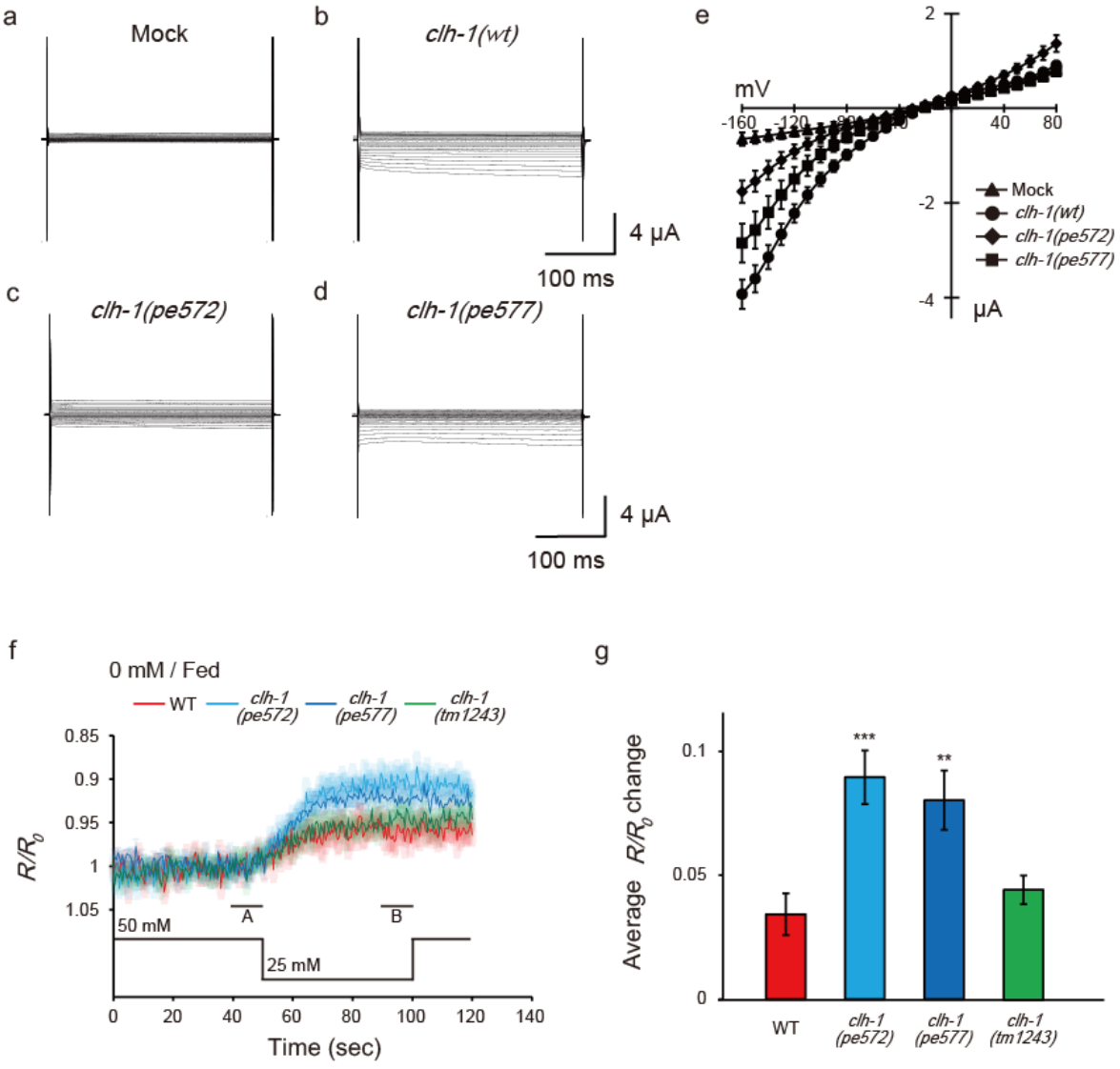

533

534 **Figure 4**

535 Mutations in *clh-1* change chloride dynamics of ASER in response to salt down-step stimulus

536 (**a-e**) Representative current traces from *Xenopus* oocytes that express cRNA for mock (**a**), *clh-*
537 *1(wt)* (**b**), *clh-1(pe572)* (**c**), *clh-1(pe577)* (**d**), clamped at voltages ranging from -160 mV to 80
538 mV. (**e**) The averaged current-voltage relationships of mock (triangle, $n = 7$), *clh-1(wt)* (circle, n
539 $= 20$), *clh-1*(*pe572)* (diamond, $n = 13$) and *clh-1(pe577)* (square, $n = 16$). The error bars
540 represent s.e.m. (**f**) Averaged Superclomeleon responses of ASER after cultivation at 0 mM
541 NaCl in the presence of food. External NaCl concentration was shifted from 50 mM to 25 mM at
542 time 50 s. Note that the scale of the vertical axis is inverted so that increase in chloride
543 concentration is displayed as up-shift of traces. The shaded region represents s.e.m., $n \geqq 17$
544 animals. (**g**) R/R_0 changes upon salt decrease. A and B indicate the time points for calculating
545 R/R_0 changes. Mean +/- s.e.m., $n \geqq 17$ animals.
546

Figure 5

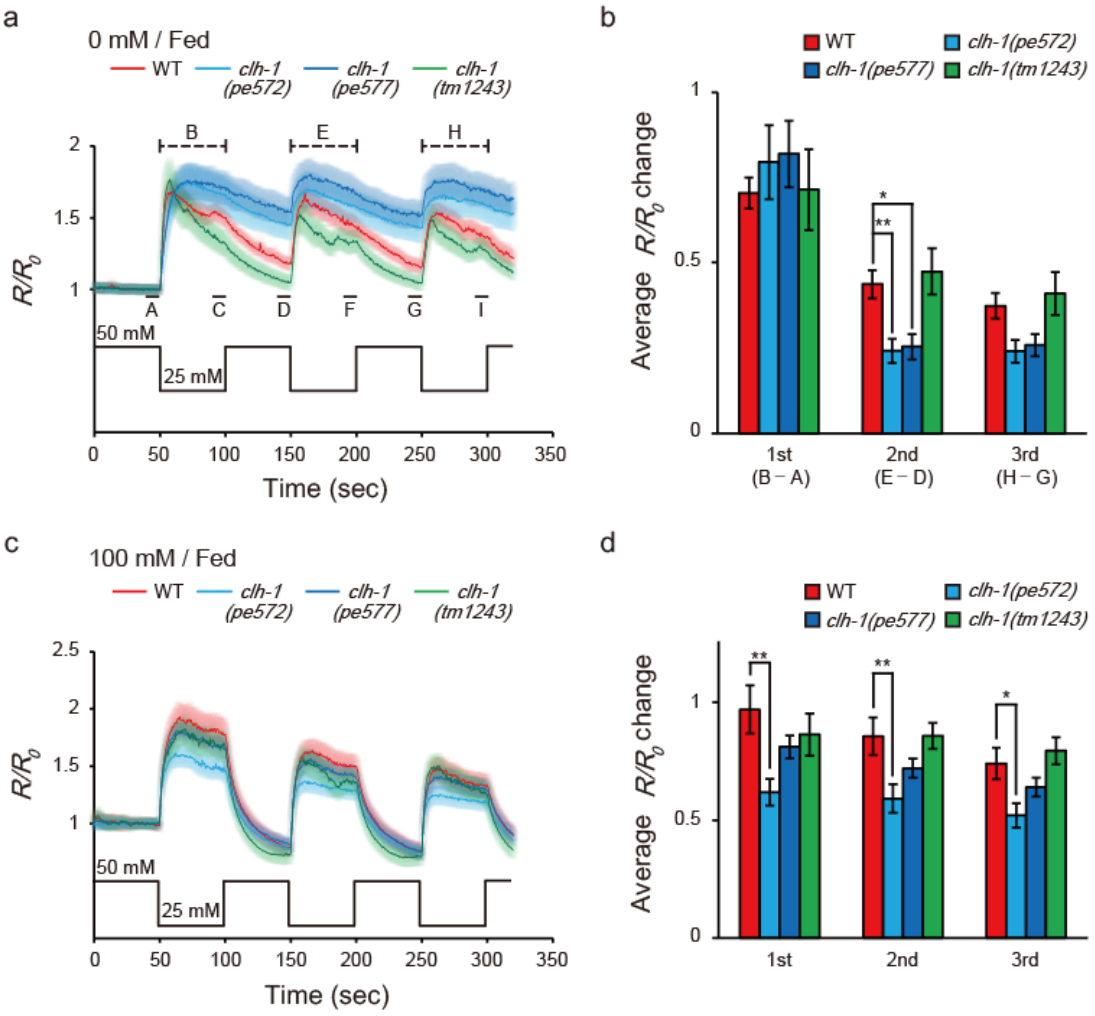

548 **Figure 5** with 2 supplements

549 Mutations in *clh-1* change calcium dynamics of ASER in response to repeated salt stimuli

550 (**a** and **c**) Averaged calcium responses of ASER after cultivation at 0 mM NaCl (**a**) or 100 mM
551 NaCl (**c**) in the presence of food, and stimulated by NaCl concentration changes between 50 mM
552 and 25 mM. A to I indicate the time points for calculation of R/R_0 intensity changes. A, D, and G
553 are the time points for pre-stimulus R/R_0, B, E, and H are the time points for peak R/R_0 during
554 stimulation, C, F, and I are the time points for decayed R/R_0 during stimulation. See methods for
555 details. The shaded region represents s.e.m., $n \geqq 16$ animals. (**b** and **d**) R/R_0 changes at each
556 NaCl down-step stimulus (B - A, E - D, and H - G for 1st, 2nd, and 3rd stimulus, respectively).
557 See methods for details. 0 mM NaCl cultivated (**b**) or 100 mM cultivated (**d**). Bar and the error
558 bar represent mean +/- s.e.m., $n \geqq 16$ animals, Dunnett's test, $^{**}p < 0.01$, $^{*}p < 0.05$.

Figure 5—figure supplement 1

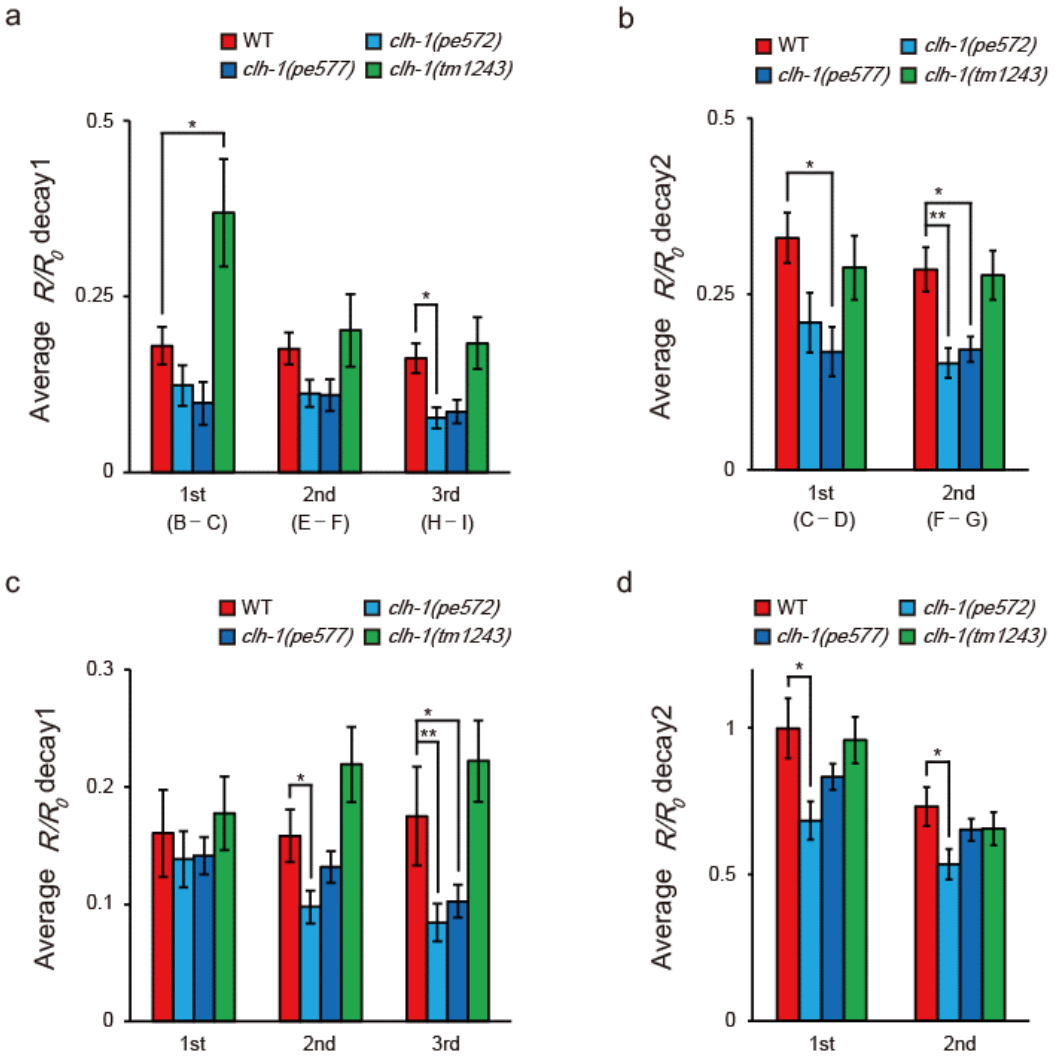

Figure 5—figure supplement 1

clh-1 missense mutations affect calcium dynamics of ASER

(**a** and **b**) Decay of ASER calcium response during 25 mM NaCl (**a**) and 50 mM NaCl (**b**). Animals were cultivated at 0 mM NaCl in the presence of food and stimulated by repeated salt concentration change as shown in Figure 5**a**. Differences of R/R_0 intensities at the time points illustrated in figure 5**a** (B to I) were calculated along with time. Calculation of "decay1" during 25 mM NaCl (**a**) was as follows; B - C for 1st, E - F for 2nd, H - I for 3rd. Calculation of "decay2" during 50 mM NaCl (**b**) was as follows; C - D for 1st, F – G for 2nd. See methods for details. Bar and the error bar represent mean +/- s.e.m., $n \geqq 16$ animals, Dunnett's test, $^{**}p < 0.01$, $^{*}p < 0.05$. (**c** and **d**) Animals were cultivated at 100 mM NaCl in the presence of food. Decays were calculated of as same as described in (**a** and **b**), see methods for details. Bar and the error bar represent mean +/- s.e.m., $n \geqq 16$ animals, Dunnett's test, $^{**}p < 0.01$, $^{*}p < 0.05$.

Figure 5—figure supplement 2

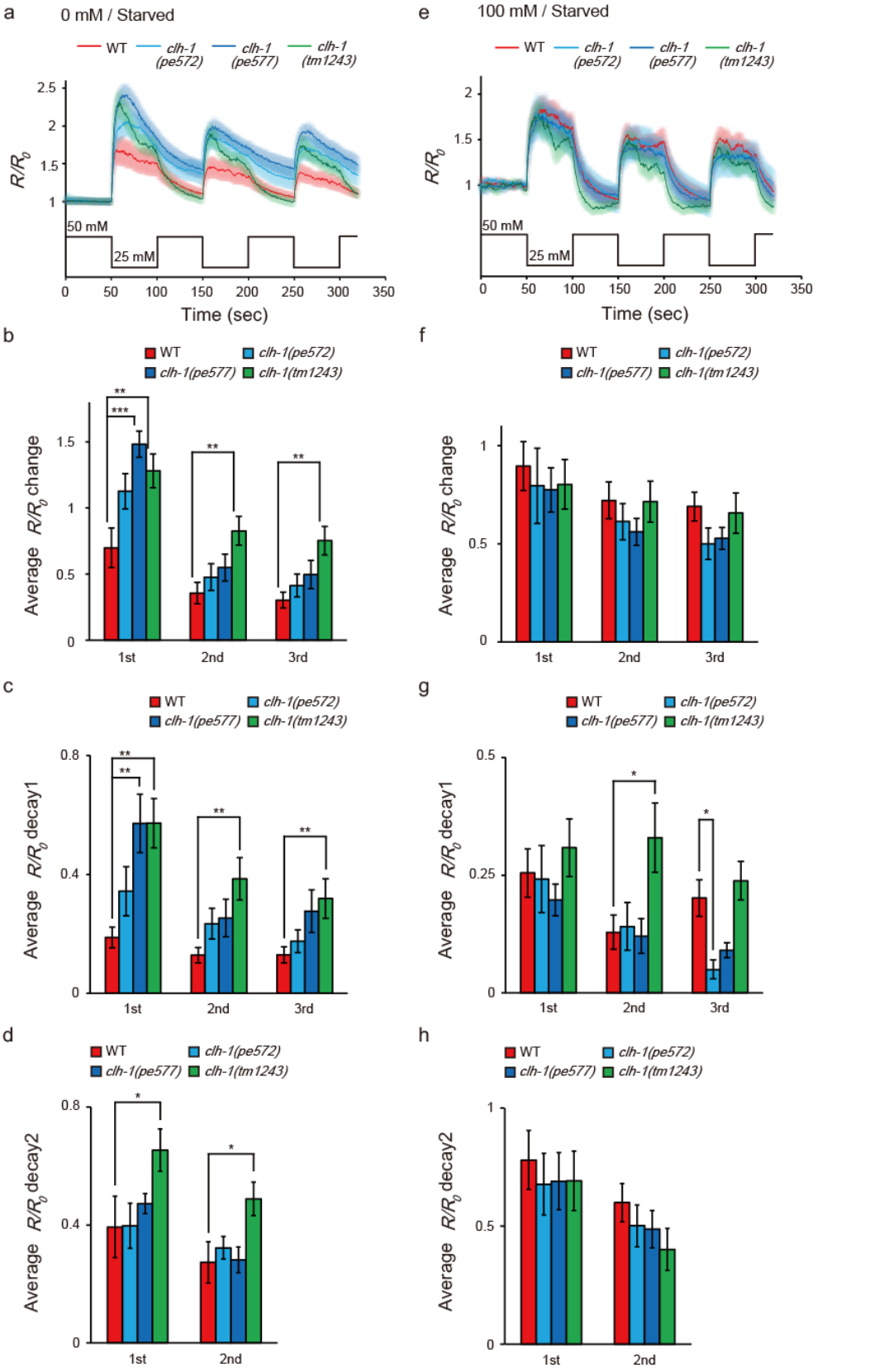

Figure 5—figure supplement 2

The *clh-1(pe)* mutations less affect calcium dynamics of ASER in starvation-experienced animals

(**a** and **b**) Calcium responses of ASER after cultivation at 0 mM NaCl (**a**) or 100 mM (**b**) in the absence of food and stimulated by NaCl concentration changes between 50 mM and 25 mM. The shaded region represents s.e.m., $n \geqq 8$ animals. (**c** to **h**) Averaged R/R_0 intensity changes at each NaCl down-step stimulus (**b**, **f**), decay of ASER calcium response during 25 mM NaCl (**c**, **g**) or 50 mM NaCl (**d**, **h**). 0 mM cultivated (**b**-**d**) or 100 mM cultivated (**f**-**h**). Calculation of R/R_0 changes and decays was performed as same as Figure 5**a** and Figure 5—figure supplement1. See methods for details. Bar and the error bar represent mean +/- s.e.m., $n \geqq 8$ animals, Dunnett's test, $^{***}p < 0.001$, $^{**}p < 0.01$, $^{*}p < 0.05$.

Figure 6

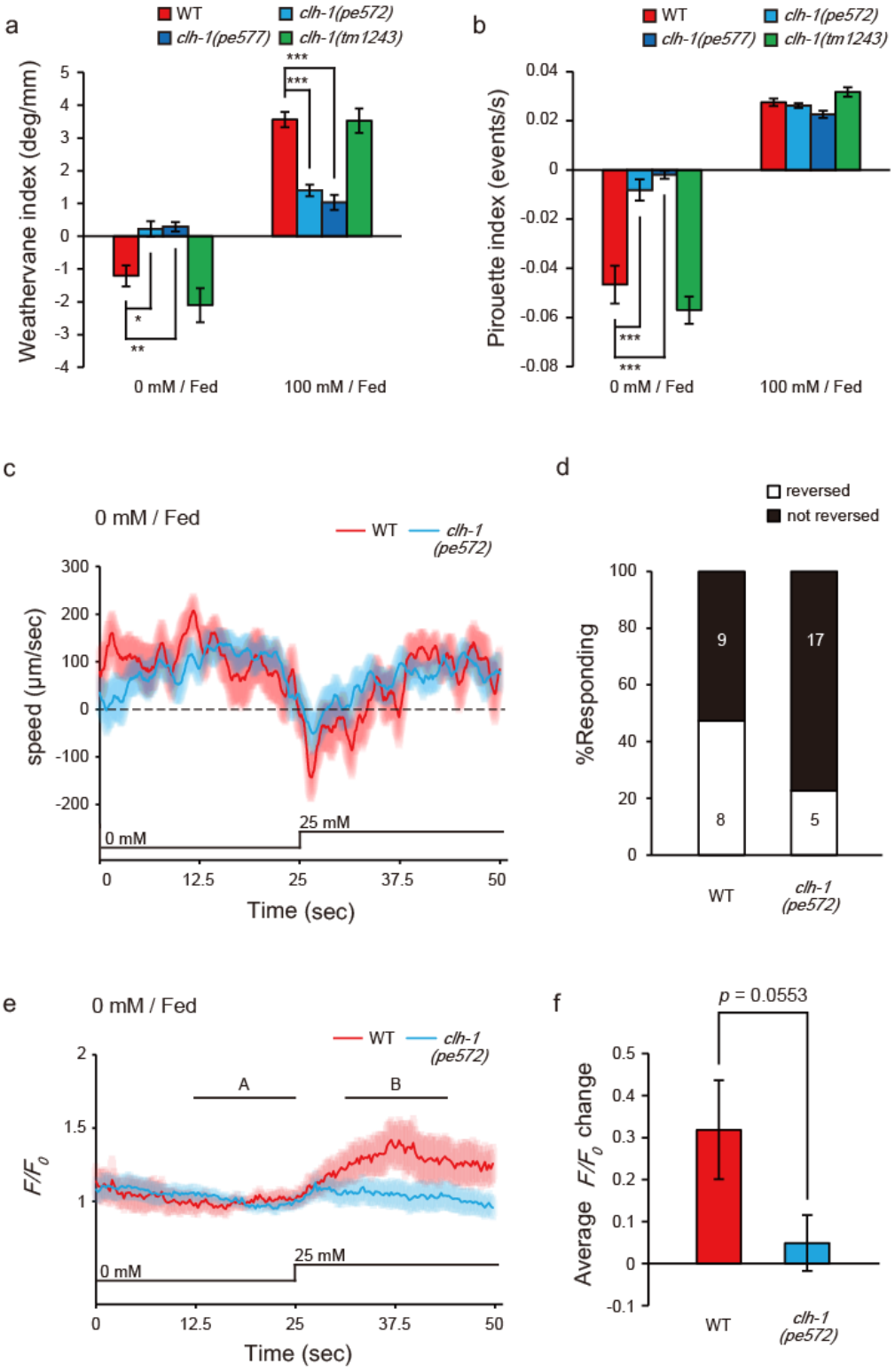

584

585 **Figure 6** with 2 supplements

586 Missense mutations in *clh-1* attenuate both klinotaxis and klinokinesis, also AIB response and
587 reversal in response to salt increase.

588 (**a** and **b**) *clh-1(pe)* mutants show defects in migration bias in salt chemotaxis. Bias of klinotaxis
589 (**a**) and klinokinesis (**b**) are represented by the weathervane index and pirouette index,
590 respectively. In both mechanisms, positive and negative indices indicate migration bias towards
591 higher and lower salt concentrations, respectively. Bar and the error bar represent mean +/-
592 s.e.m., $n \geqq 18$ assays, Dunnett's test, $***p < 0.001$, $**p < 0.01$, $*p < 0.05$. (**c** and **e**) Averaged
593 locomotion speed of animals (**c**) and GCaMP6s responses of AIB (**e**) after cultivation at 0 mM
594 NaCl in the presence of food. In (**e**), A and B indicate the time points for calculation of Averaged
595 R/R_0 changes. NaCl concentration change from 0 mM to 25 mM at 25sec. The shaded region
596 represents s.e.m., $n \geqq 19$ animals. (**d**) Proportion of animals that showed reversal after salt
597 stimulus. Reversal was defined as follows; backward locomotion, whose velocity was less than -
598 100 µm/sec, was continued for more than 1 second (35 frames). The error bars represent s.e.m., n
599 $\geqq 19$ animals, Fisher's test. (**f**) Averaged F/F_0 change (B - A, see methods). Bar and the error bar
600 represent mean +/- s.e.m., $n \geqq 19$ animals, two-tailed *t*-test with Welch's correction.

Figure 6—figure supplement 1

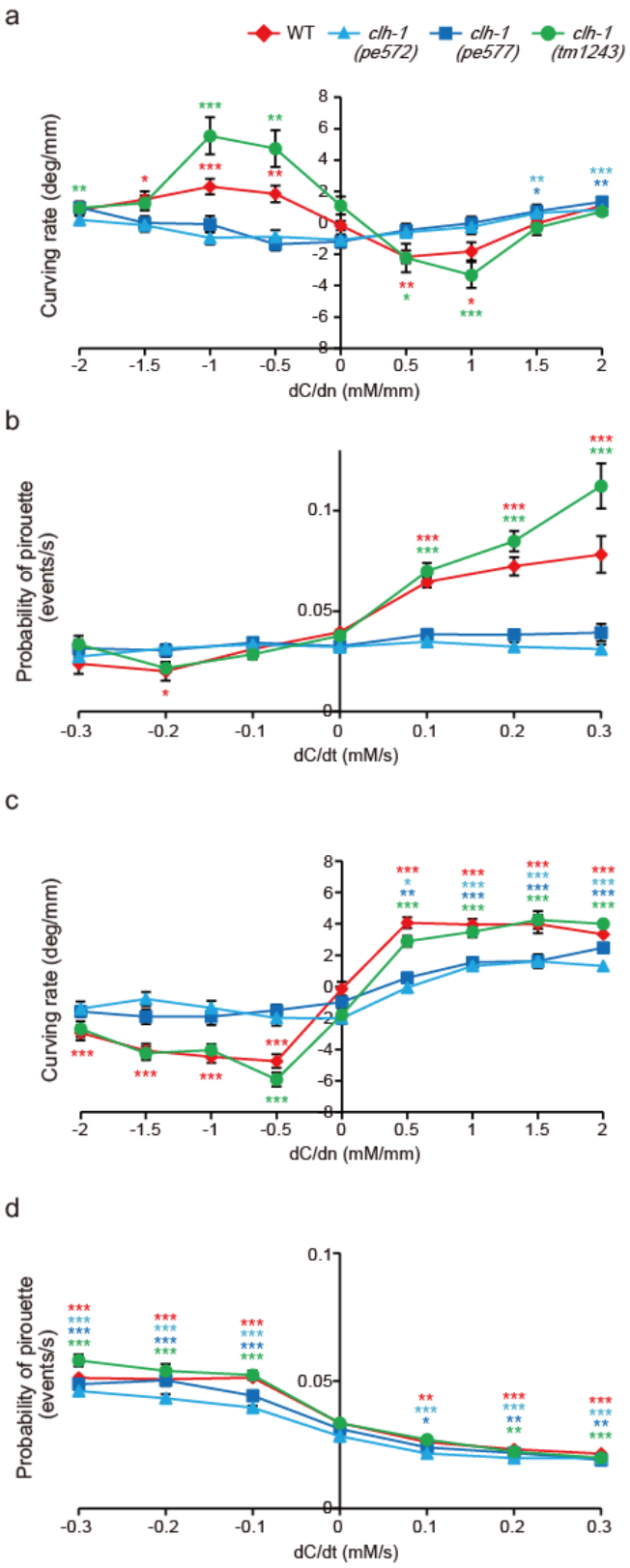

601

Figure 6—figure supplement 1

Quantification of navigation behaviors

(**a** and **b**) Chemotaxis after cultivation at 0 mM NaCl in the presence of food. Migration bias of klinotaxis is represented by curving rate (**a**) and the bias of klinokinesis is represented by probability of pirouette (**b**). dC/dn represents spatial gradient of NaCl concentration perpendicular to the direction of centroid movement of the animal. Note that migration biases in both klinotaxis and klinokinesis toward low salt are weak in the *clh-1(pe)* mutants. The error bars represent s.e.m., $n \geqq 18$ animals, compared with the basal weathervane index (dC/dn = 0) or the basal pirouette index (dC/dt = 0), Dunnett's test, $***p < 0.001$, $**p < 0.01$, $*p < 0.05$. Asterisks are colored according to the strain (red* for wild type, light blue* for *clh-1(pe572)*, deep blue* for *clh-1(pe577)*, green* for *clh-1(tm1243)*). (**c** and **d**) Chemotaxis after cultivation at 100 mM NaCl in the presence of food. Migration bias of klinotaxis (**c**) and klinokinesis (**d**). Klinotaxis, but not klinokinesis toward high salt is weak in the *clh-1(pe)* mutants. The error bars represent s.e.m., $n \geqq 19$ animals, compared with the basal weathervane index (dC/dn = 0) or the basal pirouette index (dC/dt = 0), Dunnett's test, $***p < 0.001$, $**p < 0.01$, $*p < 0.05$. Asterisks are colored according to the strain.

Figure 6—figure supplement 2

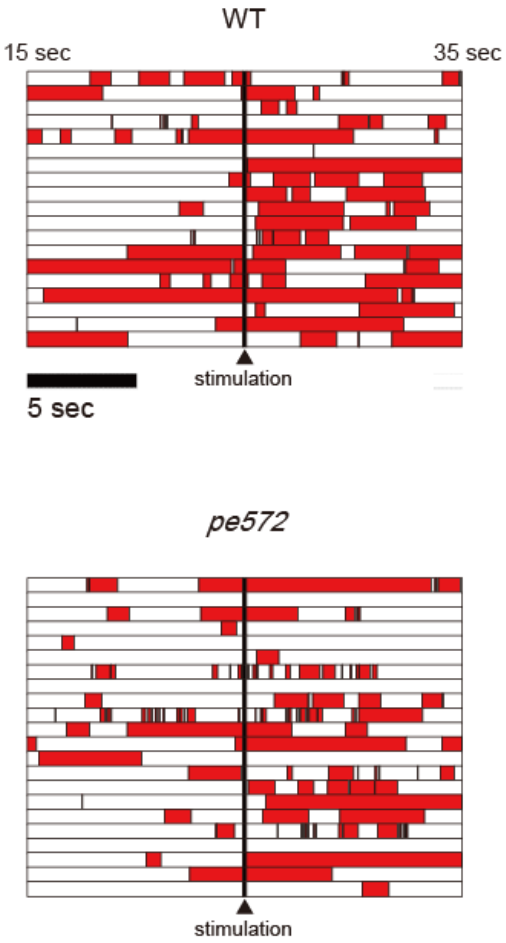

618

Figure 6—figure supplement 2

Quantification of reversal behaviors in microfluidics arena

Locomotion of wild type and *clh-1(pe572)*. Locomotion of animal was categorized as either forward (white) or reversal (red). Twenty second recordings, consisting of each 10 seconds of before and after salt up-step stimulation (arrowhead), were aligned. Each row represents each individual. $n \geqq 19$ animals.

Figure 7

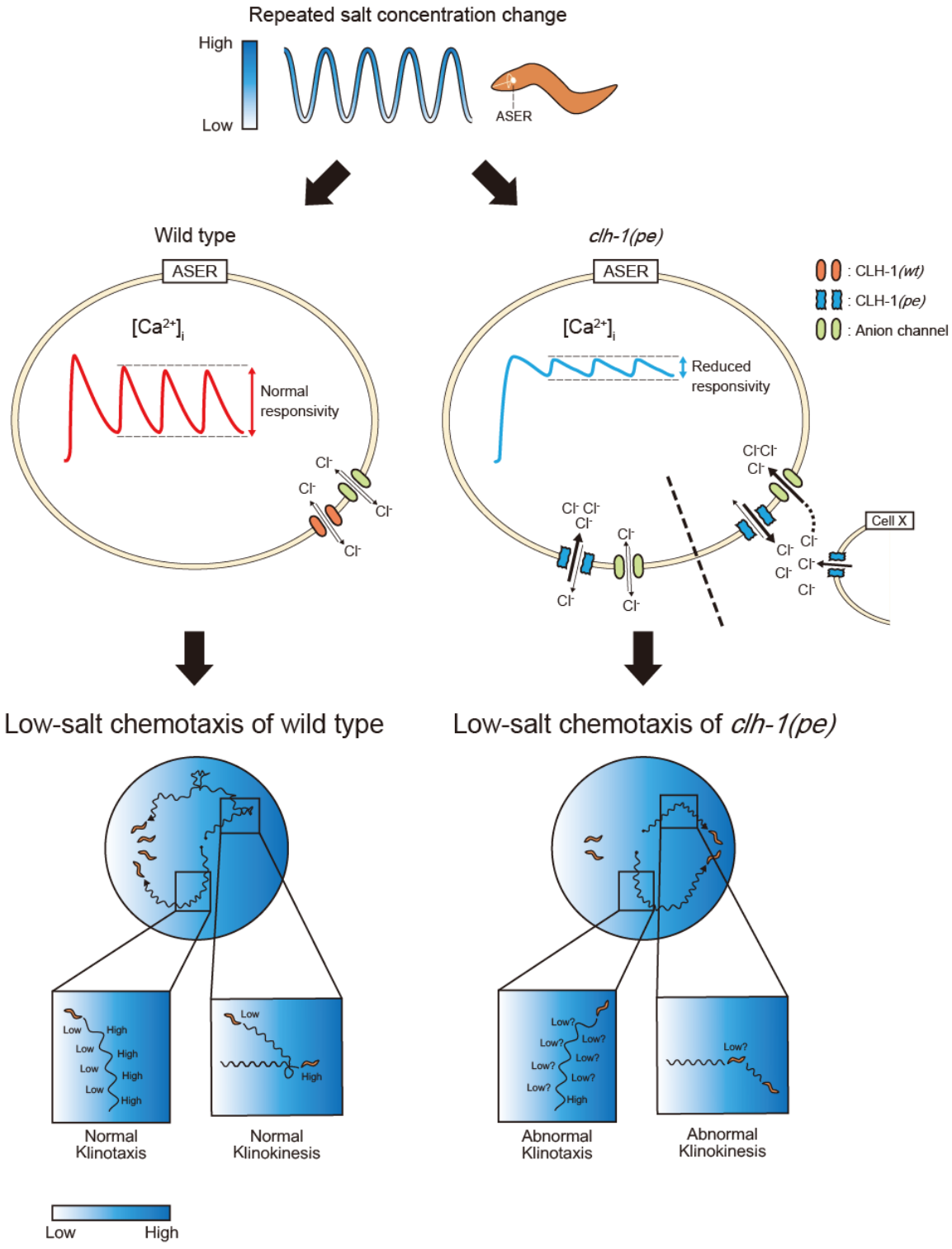

626 **Figure 7**

627 A model for the mechanism of low salt chemotaxis.

628 Animals experience salt concentration changes along with migration on salt gradient, which is
629 depicted by blue waves (top). The salt information is sensed by the ASER neuron and translated
630 into intracellular calcium transients (middle). In the *clh-1(pe)* mutants, calcium responses of
631 ASER to repeated salt stimuli is diminished after cultivation at low salt concentration. This is
632 probably due to increased chloride influx into the cell upon depolarization. Although the
633 mechanism for increased chloride influx is currently unknown, we suggest two possible
634 scenarios; increased extracellular chloride level (right) and increased chloride influx by CLH-
635 1*(pe)* (left). Reduced responsivity of ASER then results in hampered migration bias toward low
636 salt both in klinokinesis and klinotaxis (bottom).

637

Materials and methods

C. elegans strains and culture

Bristol N2 was used as wild-type *C. elegans*. All mutant strains were outcrossed multiple times with N2. *E. coli* NA22 was used as a food source for behavioral analyses including salt chemotaxis assay. For imaging experiments, OP50 was used as a food source. Strains used in this study are listed in **Supplementary file 2.**

Behavioral tests

Salt chemotaxis assays were performed as previously reported with minor modifications (Kunitomo et al., 2013). Chemotaxis assay plate was prepared as follows. On top of an agar plate (2 % agar, 25 mM potassium phosphate (pH6.0), 1 mM $CaCl_2$, 1 mM $MgSO_4$, 8.5 cm in diameter and 1.76 mm in thickness with 10 mL agar), NaCl gradient was created by placing two cylindrical agar blocks (14.5 mm in diameter and 5.3 mm in thickness) that contained 0 mM (position A) or 150 mM (position B) of NaCl in the composition of background plate. Cylindrical agar blocks were removed after 18 to 20 hours, just before assay. Animals were cultivated on regular nematode growth medium (NGM, Brenner, 1974) to young adults, and further cultivated for pre-assay cultivation on NGM plates that contained either 0 mM or 100 mM NaCl in the presence or absence of food for 6 hours. Next, fifty to two hundred worms were collected, washed twice with wash buffer (50 mM NaCl, 25 mM potassium phosphate (pH6.0), 1 mM $CaCl_2$, 1 mM $MgSO_4$, 0.02% gelatin), then placed at the center of the assay plate. Animals were allowed to run for 45 min. One microliter each of 0.5 M NaN_3 was spotted to the position A and B so that worms that had reached to these positions were immobilized. The number of

worms (*N*) within area A and B (a 2 cm radius from the center of each agar cylinder's position A and B) and area O (ellipse with radii 20 mm and 10 mm around the start point) as well as the total number of worms on assay plate were counted to calculate the chemotaxis index and immobility index as follows (Figure 1—figure 1supplement 1**a**).

$$\text{Chemotaxis index} = (N_B - N_A) / (N_{Total} - N_O)$$

$$\text{Immobility index} = N_O / N_{Total}$$

The values of chemotaxis index 1.0 and -1.0 represent complete migration towards higher and lower salt concentrations, respectively, whereas zero value represents no preference for salt concentration (unbiased migration) or a preference for concentration near the central region. Levamisole resistance was determined on agar plates that contained 0.5 mM drug at room temperature. Body paralysis was defined as the lack of body movement in response to prodding by toothpick by visual inspection every 15 min (Gottschalk et al., 2005; Lewis et al., 1980).

Forward genetic screening and identification of the responsible gene

Wild-type animals were mutagenized with ethyl methanesulfonate (EMS) as described (Brenner, 1974). Progenies were tested for food-associated salt concentration chemotaxis and mutants were selected; worms that showed defective chemotaxis were collected from the assay plate and propagated for testing at the next generation. This process was repeated until F6. We screened approximately 24,000 F2 animals and obtained 7 independent mutants. After being outcrossed with N2, two mutant strains JN572 and JN577 were further analyzed. Other mutants will be described elsewhere.

We mapped the responsible gene for JN572 and JN577, each respectively appeared to be *clh-1(pe572)* and *clh-1(pe577)* (see text), by using single nucleotide polymorphisms (SNPs) between N2 and CB4856 (Fay and Bender, 2006; Wicks et al., 2001) Both of these mutations were mapped between 2.82 (SNP: *WBVar00175127*) and 6.12 (SNP: *WBVar00176673*) on chromosome II. Genome sequences identified a missense mutation in *clh-1* in each strain. We performed rescue experiments using fosmids and genomic PCR fragment of candidate genes. Both mutants were successfully rescued by WRM0612bF09 (fosmid) or genomic PCR fragment of *clh-1*/T27D12.2. Thus we concluded *clh-1* was the causative gene. *pe572* was a G to A transition, whose 5′ and 3′ flanking sequences are TGCACATTCTCGGCGCCTAT and GGAGGTAGGGCTTAACCCTT, respectively. *pe577* was a T to C transition, whose 5′ and 3′ flanking sequences are GATTTTCATCGATATGGGAA and TGAGTATCTGATTCATTGTG, respectively.

Genotyping

Alleles of each gene locus were verified by PCR using sequence-specific primers for the target sequences. Genotyping primers used in this study are listed in **Supplementary file 3**.

clh-1 expression constructs

Full length *clh-1a*/T27D12.2a cDNA clones for wild type, *clh-1(pe572)* and *clh-1(pe577)* mutants were obtained by RT-PCR using sequence-specific primers (5′-GCTAGCCAGGATGGAAGACGCCGTCGTCGT -3′ and 5′-

GGTACCTTAGCGGGTTTCGTCATCCG -3′). PCR products were cloned to the pDEST vector (Invitrogen) as a *NheI-KpnI* fragment, and whose sequence was confirmed.

clh-1 genomic DNA fragments (*clh-1gDNA*s) were prepared by PCR using sequence-specific primers (5′- ATTGCACACATAATTGCGGTAGAC -3′ and 5′-TTGACCCATAAGGTGTAGGCTGC -3′). The nucleotide sequence of open reading frame was confirmed.

Plasmid construction

Vectors for cell-specific expression in *C. elegans* were generated using the GATEWAY system (Invitrogen). For *clh-1* promoter, a 7.5 kb DNA fragment that contains 4.0 kb upstream of transcription initiation site and 3.5 kb downstream of the first exon of *clh-1a* were amplified from *C. elegans* genome (primers: 5′- GCACACATAATTGCGGTAGAC -3′ and 5′-CGCATTTTCTTGAACCCTGG -3′), and cloned into an entry vector, pENTR-1A. For *vap-1* promoter, which specifically expresses in amphid sheath glial cells (Bacaj et al., 2008), we amplified 2.5 kb upstream of the first exon of *vap-1* (primers: 5′-ATTTATAGAAAGTTTCCAAA -3′; 5′- CTGTGAAAATGAACGCACGC -3′). pDEST-*SL2::nls4::mTFP* was generated by ligating the trans-spliced leader sequence SL2, four repeats of the nuclear localization signal, and the fluorescence protein mTFP and cloned into pDEST vector. For pDEST-*clh-1cDNA::mTFP*s, *KpnI-EcoRV* fragment from pDEST-*mTFP* was cloned into the pDEST-*clh-1cDNA* vectors. Superclomeleon (Grimley et al., 2013) was codon-optimized for expression in *C. elegans* using Codon adapter (Redemann et al., 2011), synthesized, and cloned into pDEST vector. The expression constructs pG-*clh-1p::nls4::mTFP*,

724 pG-*rimb-1p::clh-1(wt)cDNA*, pG-*gcy-5p::clh-1(wt)cDNA*, pG-*gcy-7p::clh-1(wt)cDNA*, pG-*dyf-*
725 *11p::clh-1(wt)cDNA*, pG-*vap-1p::clh-1(wt)cDNA*, pG-*gcy-5p::Superclomeleon* were created by
726 site-specific recombination between pENTR and pDEST plasmids. Other plasmids have been
727 described previously and details are available upon request.

728

729 **Generation of transgenic animals**

730 Expression constructs or genomic PCR fragments were injected at 0.1–50 ng/µl along with a co-
731 injection marker (in many case pG-*myo-3p::venus* or pG-*lin-44p::GFP*, 5-10 ng/µl) and
732 pPD49.26 carrier DNA (a gift from Andrew Fire, up to 100 ng/µl). For comparison among
733 genotypes, the transgene was initially introduced into wild-type background and transferred to
734 other genetic backgrounds by cross. JN2249 was generated by injecting pG-*clh-1p::nls4::mTFP*
735 and *lin-44p::mCherry* into an expression marker strain *Is[rimb-1p::nls4::mCherry; eat-*
736 *4p::nls4::tagRFP; lin-44p::GFP]*.

737

738 **Fluorescence microscopy and measurement of sensory cilium length**

739 Day 1 adults were mounted on 5% agar and anesthetized by 10 mM NaN_3, or 100 µm
740 levamisole. Images were captured using a Leica HCX PL APO 40×/0.85 CORR CS objective or
741 an HC PL APO 63×/0.40 CS objective on a Leica TCS-SP5 confocal microscope. The length of
742 ASER sensory cilium was measured by simple neurite tracer plugin of ImageJ. All depicted
743 representative fluorescent images were Z-stacked.

744

In vivo calcium imaging and chloride imaging

Ratiometric fluorescence reporters Yellow Cameleon 2.6 and Superclomeleon were used for calcium and chloride imaging, respectively. We found no obvious defects in salt chemotaxis of the animals that carried these reporters in wild-type background. Imaging experiments were performed as described (Iwata et al., 2011; Kunitomo et al., 2013) with minor modifications. Worms were cultivated on standard NGM seeded with OP50 until adulthood and further incubated for 6 hours at distinct salt concentrations with or without food. Worms were then trapped in a polydimethylsiloxane (PDMS) microfluidics device (Chronis et al., 2007), and NaCl concentration steps were delivered to the nose tip by switching imaging solutions (25 mM potassium phosphate (pH 6.0), 1 mM $CaCl_2$, 1 mM $MgSO_4$, 0.02% gelatin, NaCl at the indicated concentrations and glycerol to adjust their osmolarity to 350 mOsm). Time-lapse imaging was conducted with a DMI 6000B microscope (Leica) equipped with an HCX PL APO 63x objective (NA, 1.40), L5 filter set (a combination of 430/40nm band-path excitation filter and a 40% transmittance ND filter at 535/40nm dichromatic mirror, Leica), DualView (Filter sets: 505dcxr with 480/40nm and 535/40nm emission filters), and ImagEM EM-CCD camera (Hamamatsu) at two frames per second. All recordings were started 3 min after mounting to stabilize the light response of animals. Fluorescence intensity of the soma was measured. The region of interest (ROI) was tracked by Track Objects function of Metamorph software (Molecular Devices). For each frame, fluorescence intensity of the ROI was calculated by subtracting the background intensity (averaged fluorescent intensity adjacent to the ROI) from the average intensity of the ROI. The ratio of YFP/CFP fluorescence was referred to as R. R_0 was defined as the average of R over 50 frames (25 sec) prior to stimulation, and the fluorescence intensity ratio relative to R_0 (R/R_0) were calculated for a series of images. For traces, R/R_0 was averaged for all worms at each

time point. The average R/R_0 change of Superclomeleon was calculated as the difference between the value of last 10 sec during 25 mM salt stimulus and that just prior to salt concentration change (Figure 4**f**; [averaged R/R_0 during B] - [averaged R/R_0 during A]). The average R/R_0 change of YC2.6 (e.g. Figure 5**b**) was calculated as the difference between the highest value of 10 sec moving average of $R/R0$ during 25 mM NaCl stimulus (R/R_0 peak) and 10 sec average of R/R_0 just prior to corresponding NaCl decrease (e.g. [averaged R/R_0 peak of B] - [averaged R/R_0 during A] for the 1st, [averaged R/R_0 peak of E] - [averaged R/R_0 during D] for the 2nd, [averaged R/R_0 peak of H] - [averaged R/R_0 during G] for the 3rd in Figure 5**a**). Note that the time point used for R/R_0 peak differs between individuals because rise speed was different between *clh-1* genotypes. R/R_0 decay1 (e.g. Figure 5—figure supplement 1**a**) was calculated as the difference between the R/R_0 peak and the average of last 10 sec R/R_0 during 25 mM NaCl stimulus (therefore just prior to 50 mM NaCl up-step; e.g. [averaged R/R_0 during B] - [averaged R/R_0 peak of C] for the 1st, [averaged R/R_0 during E] - [averaged R/R_0 peak of F] for the 2nd, [averaged R/R_0 during H] - [averaged R/R_0 peak of I] for the 3rd, in Figure 5**a**). R/R_0 decay2 (e.g. Figure 5—figure supplement 1**b**) was calculated as the difference between the average of last 10 sec R/R_0 during 25 mM NaCl stimulus and the average of last 10 sec R/R_0 during the following 50 mM NaCl period (e.g. [averaged R/R_0 during C] - [averaged R/R_0 during D] for the 1st, [averaged R/R_0 during F] - [averaged R/R_0 during G] for the 2nd, in Figure 5**a**).

Electrophysiology

We synthesized capped CLH-1 cRNAs using T7 mMESSAGE mMACHINE kit (Ambion) and purified by lithium chloride precipitation. cRNA was quantified by spectroscopy. For oocyte

preparation, we anesthetized female *X. laevis* in cold MS-222 solution, and excised lobes of ovaries from a small incision made in the posterior ventral side. Oocytes were obtained by defolliculation; incubation of ovaries in 0.2% collagenase (Wako) in modified Barth's solution (MBSH) for 2 to 5 hours. Oocytes were washed and incubated at 16°C in MBSH with 100U/ml penicillin and 0.1mg/ml streptomycin overnight. Thereafter, oocytes were injected with cRNA mix for a final amount of 40-50 ng/oocyte. Oocytes were incubated in MBSH at 16°C for 2 to 3 days before recording. Currents were measured using a two-electrode voltage-clamp amplifier Oocyte Clamp OC-725C (Warner) at room temperature. Electrodes (0.3–1 mΩ) were filled with 3 M KCl, and then oocytes were perfused in saline with the following composition (in mM): 100 NaCl, 2 KCl, 1 $CaCl_2$, 2 $MgCl_2$, 10 HEPES, pH 7. For data acquisition and analysis, pCLAMP suite of programs (Molecular Devices) were used.

Quantitative analysis of animals' behavior

Quantitative behavior analysis was conducted as described previously with modifications (Jang et al., 2019; Kunitomo et al., 2013). Briefly, animals and chemotaxis assay plates were prepared as ordinary salt chemotaxis assay except that NaN_3 was omitted. To reduce the chance of collision of worms, only 30–50 worms were placed. Images of whole assay plate were acquired for 15 min at one frame per second. Probability of pirouette and curving rate were calculated as previously described (Jang et al., 2019). Pirouette index was defined as the difference of pirouette probability between negative dC/dT rank and positive dC/dT rank. Weathervane index was defined as the slope of the regression line in relationship between NaCl gradient in normal direction and the curving rate. We exploited data in the range of -0.3 to 0.3 for dC/dT, and -2 to 2

for dC/dn because both pirouette probability and curving rate converged towards zero with high variability in the range of highly negative or positive dC/dT or dC/dn range, probably due to small number of data points at the gradient peaks. We calculated data of each plate, then showed average and s.e.m. in figures. Data from 40 to 540 sec were used to calculate the behavioral parameters because trajectories of worms were highly interrupted by collision of worms before 40 sec.

Calcium imaging of AIB in freely moving animal

Animals expressed GCaMP6s and mCherry in AIB (JN3329, see **Supplementary file 2**). Worms were cultivated on standard NGM until young adulthood and further incubated overnight on NGM plates with 0 mM NaCl. 20~25 worms were washed out from the plate, and injected into a PDMS microfluidic device (Albrecht and Bargmann, 2011). After few minutes of acclimation to the PDMS environment under continuous flow of imaging solution without NaCl (see ***In vivo* calcium imaging and chloride imaging** for composition), a 25 mM NaCl up-step was delivered to worms. Bright-field images for locomotion analysis were acquired at 33 frames per second and fluorescence images for AIB activity were acquired at 4 frames per second with a BX51 microscope (Olympus) equipped with a halogen light source (U-LH100IR), a motorized stage (HV-STU02- 1, HawkVision), an LMPlanF1 5x objective (NA, 0.13), U-25ND25 (Olympus), a combination of 480/40nm band-path excitation filter and a 25% transmittance ND filter at 505/40nm dichromatic mirror (Leica), DualView (Filter sets: 565dcxr with 520/30nm and 630/50nm emission filters), and a CCD camera (GRAS-c3K2M-C, Point Grey Research). Tracking of particular animal was performed using a Linux-based software (Satoh et al., 2014).

Average fluorescence intensity of GCaMP6s and mCherry of the soma were determined by correcting the position of region of interest. After subtracting background, fluorescent intensity of GCaMP6s was normalized by that of mCherry. Average fluorescence intensity over 50 frames (12.5 sec) prior to stimulation was set as F_0 and the fluorescence intensity relative to F_0 (F/F_0) were calculated for a series of images. For traces, F/F_0 was averaged for all worms at each time point. The F/F_0 change in response to stimulation, we calculated the difference of averaged F/F_0 between 125 to 175 frames for peak and 51 to 100 frames for baseline (i.e. [averaged F/F_0 during B] - [averaged F/F_0 during A] in Figure 6**e**). Reversal was defined as backward movement whose averaged velocity was less than 0 µm/s (Figure 6—figure supplement 2, colored in red). In Figure 6**d**, animals those showed obvious reversal response (reversed longer than 35 frames (1 sec) within 105 frames (3 sec) after salt up-step stimulus at velocity less than -100 µm/s) were counted as "reversed animals" to exclude short spontaneous reversals that occur independent of salt stimulus (Figure 6—figure supplement 2, short red bouts).

Data analyses

The sample sizes were experimentally determined, with referring to those previously reported. Repeats of most experiments were performed in three to six separate days. Statistical analyses were performed using Prism v.5 (GraphPad software, San Diego, CA).

Supplementary file 2: Strains used in this study

Strain	Genotype	Source
N2	*C. elegans* wild type.	CGC
JN572	*clh-1(pe572) II.*	This study
JN577	*clh-1(pe577) II.*	This study
JN1638	*clh-1(tm1243) II.*	CGC [(a)]
JN1639	*clh-1(ok658) II.*	CGC [(a)]
JN2285	*clh-1(qa901) II*	CGC [(a)]
PD4788	*mIs13 I.*	From M. Edgley (Rea et al., 2005)
JN2376	*Ex[myo-3p::Venus].*	This study
JN1644	*clh-1(pe572) II; Ex[myo-3p::Venus].*	This study
JN1645	*clh-1(pe577) II; Ex[myo-3p::Venus].*	This study
-	*Ex[clh-1(wt)gDNA; myo-3p::venus].*	This study
-	*clh-1(pe572) II; Ex[clh-1(wt)gDNA; myo-3p::venus].*	This study
-	*clh-1(pe577) II; Ex[clh-1(wt)gDNA; myo-3p::venus].*	This study
JN2230	*mIs13 I; clh-1(tm1243) II.*	This study
CB1072	*unc-29(e1072) I.*	CGC
JN2207	*clh-1(tm1243) II; Ex[myo-3p::venus].*	This study
JN2263	*peEx2263[clh-1(pe572)gDNA; myo-3p::venus].*	This study
JN2265	*clh-1(tm1243) II; peEx2263[clh-1(pe572)gDNA; myo-3p::venus].*	This study
JN2267	*peEx2267[clh-1(pe577)gDNA; myo-3p::venus].*	This study
JN2269	*clh-1(tm1243) II; peEx2267[clh-1(pe577)gDNA; myo-3p::venus].*	This study
JN2231	*clh-2(ok636) II.*	CGC [(a)]
JN2260	*clh-3(ok763) II.*	CGC [(a)]
JN2286	*clh-4(ok1162) II.*	CGC [(a)]
JN2261	*clh-5(tm6008) II.*	CGC [(a)]
JN2262	*clh-6(tm617) V.*	CGC [(a)]
JN2250	*clh-2(ok636) clh-1(tm1243) II.*	This study
JN2288	*clh-3(ok763) clh-2(ok636) clh-1(tm1243) II.*	This study
JN2289	*clh-2(ok636) clh-1(tm1243) II; clh-4(ok1162) X.*	This study
JN2290	*clh-5(tm6008) clh-2(ok636) clh-1(tm1243) II.*	This study
JN2291	*clh-2(ok636) clh-1(tm1243) II; clh-6(tm617) V.*	This study
JN2325	*clh-3(ok763) clh-2(ok636) clh-1(tm1243) II; clh-4(ok1162) X.*	This study

JN2326	*clh-3(ok763) clh-5(tm6008) clh-2(ok636) clh-1(tm1243) II.*	This study
JN2249	*Is[rimb-1p::nls4::mCherry; eat-4p::nls4::tagRFP; lin-44p::GFP]; peEx2249[clh-1p::nls4::mTFP; lin-44p::mCherry].*	This study
JN2241	*clh-1(pe572) II; peEx2241[rimb-1p::clh-1(wt)cDNA; myo-3p::Venus].*	This study
JN2243	*clh-1(pe572) II; peEx2243[gcy-5p::clh-1(wt)cDNA; myo-3p::Venus].*	This study
JN2244	*clh-1(pe572) II; peEx2244[gcy-7p::clh-1(wt)cDNA; myo-3p::Venus].*	This study
JN2245	*clh-1(pe572) II; peEx2245[gcy-5p::clh-1(wt)cDNA; gcy-7p::clh-1(wt)cDNA; myo-3p::Venus].*	This study
JN2242	*clh-1(pe572) II; peEx2242[dyf-11p::clh-1(wt)cDNA; myo-3p::Venus].*	This study
JN2247	*clh-1(pe572) II; peEx2247[vap-1p::clh-1(wt)cDNA; myo-3::Venus].*	This study
JN2246	*clh-1(pe572) II; peEx2246[gcy-5p::clh-1(wt)cDNA; vap-1p::clh-1(wt)cDNA; myo-3p::Venus].*	This study
JN2229	*clh-1(pe577) II; peEx2229[gcy-5p::clh-1(wt)cDNA; myo-3p::Venus].*	This study
OH3192	*ntIs1[lin-15(+); gcy-5p::GFP] V.*	CGC (Tomioka et al., 2006)
JN2377	*clh-1(pe572) II; ntIs1[lin-15(+); gcy-5p::GFP] V.*	This study
JN2378	*clh-1(pe577) II; ntIs1[lin-15(+); gcy-5p::GFP] V.*	This study
JN2379	*clh-1(tm1243) II; ntIs1[lin-15(+); gcy-5p::GFP] V.*	This study
JN2215	*ntIs1[lin-15(+); gcy-5p::GFP] V; peEx2215[vap-1::mCherry].*	This study
JN2217	*clh-1(pe577) II; ntIs1[lin-15(+); gcy-5p::GFP] V ; peEx2215[vap-1p::mCherry].*	This study
JN2218	*clh-1(tm1243) II; ntIs1[lin-15(+); gcy-5p::GFP] V ; peEx2215[vap-1p::mCherry].*	This study
JN2255	*clh-1(pe572) II; peEx2255[lin-44p::GFP].*	This study
JN2248	*clh-1(pe572) II; peEx2248[gcy-5p::clh-1(wt)cDNA::mTFP; lin-44p::GFP].*	This study
JN2222	*peEx2222[gcy-5p::clh-1(wt)cDNA::mTFP; lin-44p::GFP].*	This study
JN2256	*clh-1(pe572) II; peEx2223[gcy-5p::clh-1(pe572)cDNA::mTFP; lin-44p::GFP].*	This study
JN2102	*Ex[gcy-5p::YC2.60; lin-44p::mCherry].*	(Jang et al., 2019)
JN2219	*clh-1(pe572) II; Ex[gcy-5p::YC2.60; lin-44p::mCherry].*	This study
JN2220	*clh-1(pe577) II; Ex[gcy-5p::YC2.60; lin-44p::mCherry].*	This study
JN2221	*clh-1(tm1243) II; Ex[gcy-5p::YC2.60; lin-44p::mCherry].*	This study
JN2321	*peEx2321[gcy-5p::CeSuperclomeleon; lin-44p::mCherry]*	This study
JN2322	*clh-1(pe572) II; peEx2321[gcy-5p::CeSuperclomeleon; lin-44p::mCherry]*	This study
JN2323	*clh-1(pe577) II; peEx2321[gcy-5p::CeSuperclomeleon; lin-44p::mCherry]*	This study
JN2324	*clh-1(tm1243) II; peEx2321[gcy-5p::CeSuperclomeleon; lin-44p::mCherry]*	This study
JN3329	*Ex[npr-9p::GCaMP6s; npr-9p::mCherry; lin-44p::GFP]*	This study
JN2345	*clh-1(pe572); Ex[npr-9p::GCaMP6s; npr-9p::mCherry; lin-44p::GFP]*	This study

a: These strains were outcrossed to N2 four to eight times in our lab before use.

Supplementary file 3: Genotyping primers used in this study

Primer name		Primer Sequence 5' → 3'
clh-1(pe572)	F [a]	CTTGCACATTCTCGGCGCATAT
clh-1(pe572)	R [a]	GCAGGTAGTGGCAAAGAATG
clh-1(pe577)	F	TTGTCGAGGACTGGTTCATC
clh-1(pe577	R	GACTCACAATCAGATACTGA
clh-1(tm1243)	F1	TGGTGTGCTATGGATTTGGA
clh-1(tm1243)	F2	TTTGTTGTCGAGGAATTGCC
clh-1(tm1243)	R	CGAAGAGAGCTCCGAGAAGA
clh-1(ok658)	F1	CCTCAGCACCTCCCCAAATTA
clh-1(ok658)	F2	CCGAAACTTCATGCTAGAGTC
clh-1(ok658)	R	AAAACCCCAAACCCAAAATC
clh-1(qa901)	F1	CCTAGTAAAGAGGCAGGTACGTG
clh-1(qa901)	F2	CCAACTGTACCCTCTGGAAGC
clh-1(qa901)	R	CGGCATAAAGTCCAGGGTAGATC
clh-2(ok636)	F1	CTTCCTCGCCTTCACTGTGTTC
clh-2(ok636)	F2	TGGTAAACCAGCAGGACAGTCG
clh-2(ok636)	R1	GGCAATGGAGAGGAGATATTGAGAG
clh-3(ok763)	F1	CCCATCTTCATCGCCACTTTC
clh-3(ok763)	F2	CGTACTGAATGGGAGGATATGATG
clh-3(ok763)	R	CCCATCTTCATCGCCACTTTC
clh-4(ok1162) [b]	F	GTCAGCGCGTTCTACCAAACAAG
clh-4(ok1162) [b]	R1	GCTCCGCAAACAAGATCATCTGAC
clh-4(ok1162) [b]	R2	CAAGCCAAAGATCCTGAATGCTCC
clh-5(tm6008)	F1	GGAGATCATTCTTCTGTGCATTGG
clh-5(tm6008)	F2	CTTCTCTGGTCCTCTCGTAAC
clh-5(tm6008)	R	GCGTGATTAGCATGACTTCGTAG

clh-6(tm617)	F1	GCTCCAAGACAGCCTCCAATTATTC
clh-6(tm617)	F2	CCTATCCAAGCTATCATTACGGTCCAC
clh-6(tm617)	R	CTGGACTCGTCGCTGCATTTATTG

a: F signifies forward and R signifies reverse.

b: in *clh-4(ok1162)*, it has revealed by sequencing that 2.6 kb between exon7 and exon 18 were substituted to another 1.4 kb sequence in the allele, which mutation presumably destroy the function of CLH-4 protein.

853

854

Acknowledgments

We thank the Caenorhabditis Genetics Center (CGC) and the National Bioresource Project (NBRP) for strains; Ishihara T. for pDEST-*nls-YC2.60*, Oka Y. and for electrophysiology setup and technical assistance, Chronis N., Albrecht D. and Bargmann C. for design of microfluidics chips. We also thank members of the Iino laboratory members for helpful comments and discussion.

References

Accardi A. 2015. Structure and gating of CLC channels and exchangers. *J Physiol* **593**:4129–4138. doi:10.1113/JP270575

Adachi T, Kunitomo H, Tomioka M, Ohno H, Okochi Y, Mori I, Iino Y. 2010. Reversal of salt preference is directed by the insulin/PI3K and G q/PKC signaling in Caenorhabditis elegans. *Genetics*. doi:10.1534/genetics.110.119768

Adrian RH, Bryant SH. 1974. On the repetitive discharge in myotonic muscle fibres. *J Physiol*. doi:10.1113/jphysiol.1974.sp010620

Ahnert-Hilger G, Jahn R. 2011. CLC-3 spices up GABAergic synaptic vesicles. *Nat Neurosci*. doi:10.1038/nn.2786

Albrecht DR, Bargmann CI. 2011. High-content behavioral analysis of Caenorhabditis elegans in precise spatiotemporal chemical environments. *Nat Methods*. doi:10.1038/nmeth.1630

874 Schriever AM, Friedrich T, Pusch M, Jentsch TJ. 1999. CLC chloride channels in Caenorhabditis
875 elegans. *J Biol Chem*. doi: 10.1074/jbc.274.48.34238

876 Bacaj T, Tevlin M, Lu Y, Shaham S. 2008. Glia are essential for sensory organ function in C.
877 elegans. *Science* **322**:744–7. doi:10.1126/science.1163074

878 Bargmann CI. 1998. Neurobiology of the Caenorhabditis elegans genome. *Science (80-).*
879 doi:10.1126/science.282.5396.2028

880 Bargmann CI, Horvitz HR. 1991. Chemosensory neurons with overlapping functions direct
881 chemotaxis to multiple chemicals in C. elegans. *Neuron* **7**:729–742. doi:10.1016/0896-
882 6273(91)90276-6

883 Blanz J, Schweizer M, Auberson M, Maier H, Muenscher A, Hübner CA, Jentsch TJ. 2007.
884 Leukoencephalopathy upon disruption of the chloride channel ClC-2. *J Neurosci*.
885 doi:10.1523/JNEUROSCI.0338-07.2007

886 Bösl MR, Stein V, Hübner C, Zdebik AA, Jordt SE, Mukhopadhyay AK, Davidoff MS, Holstein
887 AF, Jentsch TJ. 2001. Male germ cells and photoreceptors, both dependent on close cell-cell
888 interactions, degenerate upon ClC-2 Cl- channel disruption. *EMBO J*.
889 doi:10.1093/emboj/20.6.1289

890 Branicky R, Miyazaki H, Strange K, Schafer WR. 2014. The voltage-gated anion channels
891 encoded by clh-3 regulate egg laying in C. elegans by modulating motor neuron excitability.
892 *J Neurosci*. doi:10.1523/JNEUROSCI.3112-13.2014

893 Braubach OR, Wood HD, Gadbois S, Fine A, Croll RP. 2009. Olfactory conditioning in the
894 zebrafish (Danio rerio). *Behav Brain Res*. doi:10.1016/j.bbr.2008.10.044

Brenner S. 1974. The genetics of Caenorhabditis elegans. *Genetics* **77**:71–94. doi:10.1002/cbic.200300625

Chalasani SH, Chronis N, Tsunozaki M, Gray JM, Ramot D, Goodman MB, Bargmann CI. 2007. Dissecting a circuit for olfactory behaviour in Caenorhabditis elegans. *Nature*. doi:10.1038/nature06292

Charlet-B. N, Savkur RS, Singh G, Philips A V., Grice EA, Cooper TA. 2002. Loss of the muscle-specific chloride channel in type 1 myotonic dystrophy due to misregulated alternative splicing. *Mol Cell*. doi:10.1016/S1097-2765(02)00572-5

Cho CE, Brueggemann C, L'Etoile ND, Bargmann CI. 2016. Parallel encoding of sensory history and behavioral preference during Caenorhabditis elegans olfactory learning. *Elife*. doi:10.7554/eLife.14000

Chronis N, Zimmer M, Bargmann CI. 2007. Microfluidics for in vivo imaging of neuronal and behavioral activity in Caenorhabditis elegans. *Nat Methods*. doi:10.1038/nmeth1075

Colbert HA, Bargmann CI. 1995. Odorant-specific adaptation pathways generate olfactory plasticity in C. elegans. *Neuron*. doi:10.1016/0896-6273(95)90224-4

Deidda G, Parrini M, Naskar S, Bozarth IF, Contestabile A, Cancedda L. 2015. Reversing excitatory GABA A R signaling restores synaptic plasticity and memory in a mouse model of Down syndrome. *Nat Med*. doi:10.1038/nm.3827

Dutzler R, Campbell EB, Cadene M, Chait BT, MacKinnon R. 2002. X-ray structure of a CIC chloride channel at 3.0 Å reveals the molecular basis of anion selectivity. *Nature*. doi:10.1038/415287a

916 Fahlke C, Riidel R, Mitrovic N, Zhou M, George AL. 1995. An aspartic acid residue important
917 for voltage-dependent gating of human muscle chloride channels. *Neuron*.
918 doi:10.1016/0896-6273(95)90050-0

919 Fay D, Bender A. 2006. Genetic mapping and manipulation: chapter 4--SNPs: introduction and
920 two-point mapping. *WormBook*. doi:10.1895/wormbook.1.93.1

921 Fernandes-Rosa FL, Daniil G, Orozco IJ, Göppner C, El Zein R, Jain V, Boulkroun S,
922 Jeunemaitre X, Amar L, Lefebvre H, Schwarzmayr T, Strom TM, Jentsch TJ, Zennaro MC.
923 2018. A gain-of-function mutation in the CLCN2 chloride channel gene causes primary
924 aldosteronism. *Nat Genet* **50**:1–7. doi:10.1038/s41588-018-0053-8

925 Goodman MB, Hall DH, Avery L, Lockery SR. 1998. Active currents regulate sensitivity and
926 dynamic range in C. elegans Neurons. *Neuron*. doi:10.1016/S0896-6273(00)81014-4

927 Gordus A, Pokala N, Levy S, Flavell SW, Bargmann CI. 2015. Feedback from network states
928 generates variability in a probabilistic olfactory circuit. *Cell*. doi:10.1016/j.cell.2015.02.018

929 Gottfried JA, O'Doherty J, Dolan RJ. 2003. Encoding predictive reward value in human
930 amygdala and orbitofrontal cortex. *Science (80-).* doi:10.1126/science.1087919

931 Gottschalk A, Almedom RB, Schedletzky T, Anderson SD, Yates JR, Schafer WR. 2005.
932 Identification and characterization of novel nicotinic receptor-associated proteins in
933 Caenorhabditis elegans. *EMBO J*. doi:10.1038/sj.emboj.7600741

934 Grant J, Matthewman C, Bianchi L. 2015. A Novel Mechanism of pH Buffering in *C. elegans*
935 Glia: Bicarbonate Transport via the Voltage-Gated ClC Cl- Channel CLH-1. *J Neurosci*
936 **35**:16377–16397. doi:10.1523/JNEUROSCI.3237-15.2015

937 Gray JM, Hill JJ, Bargmann CI. 2005. A circuit for navigation in Caenorhabditis elegans. *Proc*
938 *Natl Acad Sci U S A*. doi:10.1073/pnas.0409009101

939 Grimley JS, Li L, Wang W, Wen L, Beese LS, Hellinga HW, Augustine GJ. 2013. Visualization
940 of synaptic inhibition with an optogenetic sensor developed by cell-free protein engineering
941 automation. *J Neurosci*. doi:10.1523/JNEUROSCI.4616-11.2013

942 Hedgecock EM, Russell RL. 1975. Normal and mutant thermotaxis in the nematode
943 Caenorhabditis elegans. *Proc Natl Acad Sci U S A*. doi:10.1073/pnas.72.10.4061

944 Hirano Y, Masuda T, Naganos S, Matsuno M, Ueno K, Miyashita T, Horiuchi J, Saitoe M. 2013.
945 Fasting launches CRTC to facilitate long-term memory formation in Drosophila. *Science*
946 *(80-)*. doi:10.1126/science.1227170

947 Horikawa K, Yamada Y, Matsuda T, Kobayashi K, Hashimoto M, Matsu-Ura T, Miyawaki A,
948 Michikawa T, Mikoshiba K, Nagai T. 2010. Spontaneous network activity visualized by
949 ultrasensitive Ca 2+ indicators, yellow Cameleon-Nano. *Nat Methods*.
950 doi:10.1038/nmeth.1488

951 Iino Y, Yoshida K. 2009. Parallel use of two behavioral mechanisms for chemotaxis in
952 Caenorhabditis elegans. *J Neurosci* **29**:5370–5380. doi:10.1523/JNEUROSCI.3633-08.2009

953 Iwata R, Oda S, Kunitomo H, Iino Y. 2011. Roles for class IIA phosphatidylinositol transfer
954 protein in neurotransmission and behavioral plasticity at the sensory neuron synapses of
955 Caenorhabditis elegans. *Proc Natl Acad Sci U S A*. doi:10.1073/pnas.1016232108

Jang MS, Toyoshima Y, Tomioka M, Kunitomo H, Iino Y. 2019. Multiple sensory neurons mediate starvation-dependent aversive navigation in Caenorhabditis elegans. *Proc Natl Acad Sci U S A*. doi:10.1073/pnas.1821716116

Jentsch TJ. 2008. CLC chloride channels and transporters: From genes to protein structure, pathology and physiology. *Crit Rev Biochem Mol Biol*. doi:10.1080/10409230701829110

Jentsch TJ. 2007. Chloride and the endosomal-lysosomal pathway: Emerging roles of CLC chloride transporters. *J Physiol*. doi:10.1113/jphysiol.2006.124719

Jeworutzki E, Lagostena L, Elorza-Vidal X, López-Hernández T, Estévez R, Pusch M. 2014. GlialCAM, a CLC-2 Cl- channel subunit, activates the slow gate of CLC chloride channels. *Biophys J*. doi:10.1016/j.bpj.2014.07.040

Kindt KS, Quast KB, Giles AC, De S, Hendrey D, Nicastro I, Rankin CHH, Schafer WR. 2007. Dopamine Mediates Context-Dependent Modulation of Sensory Plasticity in C. elegans. *Neuron*. doi:10.1016/j.neuron.2007.07.023

Kunitomo H, Sato H, Iwata R, Satoh Y, Ohno H, Yamada K, Iino Y. 2013. Concentration memory-dependent synaptic plasticity of a taste circuit regulates salt concentration chemotaxis in *Caenorhabditis elegans*. *Nat Commun* **4**:2210. doi:10.1038/ncomms3210

Kuramochi M, Doi M. 2019. An excitatory/inhibitory switch from asymmetric sensory neurons defines postsynaptic tuning for a rapid response to NaCl in Caenorhabditis elegans. *Front Mol Neurosci*. doi:10.3389/fnmol.2018.00484

Lewis JA, Wu CH, Berg H, Levine JH. 1980. The genetics of levamisole resistance in the nematode Caenorhabditis elegans. *Genetics*. vol. 95 no. 4 905-928

977 Li Z, Liu J, Zheng M, Xu XZS. 2014. Encoding of both analog- and digital-like behavioral
978 outputs by one C. Elegans interneuron. *Cell*. doi:10.1016/j.cell.2014.09.056

979 Luo L, Wen Q, Ren J, Hendricks M, Gershow M, Qin Y, Greenwood J, Soucy ER, Klein M,
980 Smith-Parker HK, Calvo AC, Colón-Ramos DA, Samuel ADT, Zhang Y. 2014. Dynamic
981 encoding of perception, memory, and movement in a C. elegans chemotaxis circuit. *Neuron*.
982 doi:10.1016/j.neuron.2014.05.010

983 Nehrke K, Begenisich T, Pilato J, Melvin JE. 2000. Into ion channel and transporter function.
984 Caenorhabditis elegans ClC-type chloride channels: novel variants and functional
985 expression. *Am J Physiol Cell Physiol* **279**:C2052-66.

986 O'Doherty JP, Dayan P, Friston K, Critchley H, Dolan RJ. 2003. Temporal difference models
987 and reward-related learning in the human brain. *Neuron*. doi:10.1016/S0896-
988 6273(03)00169-7

989 Oda S, Tomioka M, Iino Y. 2011. Neuronal plasticity regulated by the insulin-like signaling
990 pathway underlies salt chemotaxis learning in Caenorhabditis elegans. *J Neurophysiol*.
991 doi:10.1152/jn.01029.2010

992 Ortiz CO, Faumont S, Takayama J, Ahmed HK, Goldsmith AD, Pocock R, McCormick KE,
993 Kunimoto H, Iino Y, Lockery S, Hobert O. 2009. Lateralized Gustatory Behavior of C.
994 elegans Is Controlled by Specific Receptor-Type Guanylyl Cyclases. *Curr Biol* **19**:996–
995 1004. doi:10.1016/j.cub.2009.05.043

Otis JM, Namboodiri VMK, Matan AM, Voets ES, Mohorn EP, Kosyk O, McHenry JA, Robinson JE, Resendez SL, Rossi MA, Stuber GD. 2017. Prefrontal cortex output circuits guide reward seeking through divergent cue encoding. *Nature*. doi:10.1038/nature21376

Pavlov IP. 1927. Classics in the History of Psychology -- Pavlov (1927) Lecture 2. *Cond REFLEXES AN Investig Physiol Act Cereb CORTEX*.

Perkins LA, Hedgecock EM, Thomson JN, Culotti JG. 1986. Mutant sensory cilia in the nematode Caenorhabditis elegans. *Dev Biol*. doi:10.1016/0012-1606(86)90314-3

Pfeffer CK, Stein V, Keating DJ, Maier H, Rinke I, Rudhard Y, Hentschke M, Rune GM, Jentsch TJ, Hübner CA. 2009. NKCC1-dependent GABAergic excitation drives synaptic network maturation during early hippocampal development. *J Neurosci*. doi:10.1523/JNEUROSCI.1377-08.2009

Pierce-Shimomura JT, Faumont S, Gaston MR, Pearson BJ, Lockery SR. 2001. The homeobox gene lim-6 is required for distinct chemosensory representations in *C. elegans*. *Nature* **410**:694–698. doi:10.1038/35070575

Piggott BJ, Liu J, Feng Z, Wescott SA, Xu XZS. 2011. The neural circuits and synaptic mechanisms underlying motor initiation in C. elegans. *Cell*. doi:10.1016/j.cell.2011.08.053

Pusch M, Steinmeyer K, Koch MC, Jentsch TJ. 1995. Mutations in dominant human myotonia congenita drastically alter the voltage dependence of the CIC-1 chloride channel. *Neuron*. doi:10.1016/0896-6273(95)90023-3

Ratté S, Prescott SA. 2011. CLC-2 channels regulate neuronal excitability, not intracellular chloride levels. *J Neurosci*. doi:10.1523/JNEUROSCI.2748-11.2011

1017 Rea SL, Wu D, Cypser JR, Vaupel JW, Johnson TE. 2005. A stress-sensitive reporter predicts
1018 longevity in isogenic populations of Caenorhabditis elegans. *Nat Genet*.
1019 doi:10.1038/ng1608

1020 Redemann S, Schloissnig S, Ernst S, Pozniakowsky A, Ayloo S, Hyman AA, Bringmann H.
1021 2011. Codon adaptation-based control of protein expression in C. elegans. *Nat Methods*.
1022 doi:10.1038/nmeth.1565

1023 Rhodes TH, Vite CH, Giger U, Patterson DF, Fahlke C, George AL. 1999. A missense mutation
1024 in canine ClC-1 causes recessive myotonia congenita in the dog. *FEBS Lett*.
1025 doi:10.1016/S0014-5793(99)00926-6

1026 Rinke I, Artmann J, Stein V. 2010. ClC-2 voltage-gated channels constitute part of the
1027 background conductance and assist chloride extrusion. *J Neurosci*.
1028 doi:10.1523/JNEUROSCI.6299-09.2010

1029 Saeki S, Yamamoto M, Iino Y. 2001. Plasticity of chemotaxis revealed by paired presentation of
1030 a chemoattractant and starvation in the nematode Caenorhabditis elegans. *J Exp Biol*. 2001
1031 204: 1757-1764

1032 Sasakura H, Mori I. 2013. Behavioral plasticity, learning, and memory in C. elegans. *Curr Opin*
1033 *Neurobiol*. doi:10.1016/j.conb.2012.09.005

1034 Satoh Y, Sato H, Kunitomo H, Fei X, Hashimoto K, Iino Y. 2014. Regulation of experience-
1035 dependent bidirectional chemotaxis by a neural circuit switch in Caenorhabditis elegans. *J*
1036 *Neurosci*. doi:10.1523/JNEUROSCI.1757-14.2014

1037 Serrano-Saiz E, Poole RJ, Felton T, Zhang F, De La Cruz ED, Hobert O. 2013. XModular
1038 control of glutamatergic neuronal identity in C. elegans by distinct homeodomain proteins.
1039 *Cell*. doi:10.1016/j.cell.2013.09.052

1040 Shindou T, Ochi-Shindou M, Murayama T, Saita E ichiro, Momohara Y, Wickens JR,
1041 Maruyama IN. 2019. Active propagation of dendritic electrical signals in C. elegans. *Sci*
1042 *Rep*. doi:10.1038/s41598-019-40158-9

1043 Singhvi A, Liu B, Friedman CJ, Fong J, Lu Y, Huang XY, Shaham S. 2016. A Glial K/Cl
1044 Transporter Controls Neuronal Receptive Ending Shape by Chloride Inhibition of an rGC.
1045 *Cell* **165**:936–948. doi:10.1016/j.cell.2016.03.026

1046 Smith HK, Luo L, O'Halloran D, Guo D, Huang XY, Samuel ADT, Hobert O. 2013. Defining
1047 specificity determinants of cGMP mediated gustatory sensory transduction in
1048 Caenorhabditis elegans. *Genetics*. doi:10.1534/genetics.113.152660

1049 Staley K, Smith R, Schaack J, Wilcox C, Jentsch TJ. 1996. Alteration of GABA(A) receptor
1050 function following gene transfer of the CLC-2 chloride channel. *Neuron*.
1051 doi:10.1016/S0896-6273(00)80186-5

1052 Staley KJ, Soldo BL, Proctor WR. 1995. Ionic mechanisms of neuronal excitation by inhibitory
1053 GABAA receptors. *Science (80-)*. doi:10.1126/science.7638623

1054 Stauber T, Weinert T, Jentsch TJ. 2012. Cell biology and physiology of CLC chloride channels
1055 and transporters. *Compr Physiol*. doi:10.1002/cphy.c110038

1056 Stölting G, Fischer M, Fahlke C. 2014a. ClC-1 and ClC-2 form hetero-dimeric channels with
1057 novel protopore functions. *Pflugers Arch Eur J Physiol*. doi:10.1007/s00424-014-1490-6

1058 Stölting G, Fischer M, Fahlke C. 2014b. CLC channel function and dysfunction in health and
1059 disease. *Front Physiol* **5**:1–18. doi:10.3389/fphys.2014.00378

1060 Summers PJ, Layne RM, Ortega AC, Harris GP, Bamber BA, Komuniecki RW. 2015. Multiple
1061 sensory inputs are extensively integrated to modulate nociception in C. elegans. *J Neurosci*.
1062 doi:10.1523/JNEUROSCI.0225-15.2015

1063 Suzuki H, Thiele TR, Faumont S, Ezcurra M, Lockery SR, Schafer WR. 2008. Functional
1064 asymmetry in Caenorhabditis elegans taste neurons and its computational role in
1065 chemotaxis. *Nature* **454**:114–7. doi:10.1038/nature06927

1066 Thiemann A, Gründer S, Pusch M, Jentsch TJ. 1992. A chloride channel widely expressed in
1067 epithelial and non-epithelial cells. *Nature*. doi:10.1038/356057a0

1068 Tomioka M, Adachi T, Suzuki H, Kunitomo H, Schafer WR, Iino Y. 2006. The Insulin/PI 3-
1069 Kinase Pathway Regulates Salt Chemotaxis Learning in Caenorhabditis elegans. *Neuron*
1070 **51**:613–625. doi:10.1016/j.neuron.2006.07.024

1071 Wang L, Sato H, Satoh Y, Tomioka M, Kunitomo X, Iino Y. 2017. A gustatory neural circuit of
1072 Caenorhabditis elegans generates memory-dependent behaviors in Na+ chemotaxis. *J*
1073 *Neurosci*. doi:10.1523/JNEUROSCI.1774-16.2017

1074 Ward S, Thomson N, White JG, Brenner S. 1975. Electron microscopical reconstruction of the
1075 anterior sensory anatomy of the nematode caenorhabditis elegans. *J Comp Neurol*.
1076 doi:10.1002/cne.901600305

1077 Ware RW, Clark D, Crossland K, Russell RL. 1975. The nerve ring of the nematode
1078 Caenorhabditis elegans: Sensory input and motor output. *J Comp Neurol*.
1079 doi:10.1002/cne.901620106

1080 Wicks SR, Yeh RT, Gish WR, Waterston RH, Plasterk RHA. 2001. Rapid gene mapping in
1081 Caenorhabditis elegans using a high density polymorphism map. *Nat Genet*.
1082 doi:10.1038/88878

1083 Winter Y, Stich KP. 2005. Foraging in a complex naturalistic environment: Capacity of spatial
1084 working memory in flower bats. *J Exp Biol*. doi:10.1242/jeb.01416

1085 Wu F-F. 2002. Novel CLCN1 mutations with unique clinical and electrophysiological
1086 consequences. *Brain* **125**:2392–2407. doi:10.1093/brain/awf246

1087 Yamamoto T, Shimojima K, Sangu N, Komoike Y, Ishii A, Abe S, Yamashita S, Imai K, Kubota
1088 T, Fukasawa T, Okanishi T, Enoki H, Tanabe T, Saito A, Furukawa T, Shimizu T, Milligan
1089 CJ, Petrou S, Heron SE, Dibbens LM, Hirose S, Okumura A. 2015. Single Nucleotide
1090 variations in CLCN6 identified in patients with benign partial epilepsies in infancy and/or
1091 febrile seizures. *PLoS One*. doi:10.1371/journal.pone.0118946

1092 Zou W, Fu J, Zhang H, Du K, Huang W, Yu J, Li S, Fan Y, Baylis HA, Gao S, Xiao R, Ji W,
1093 Kang L, Xu T. 2018. Decoding the intensity of sensory input by two glutamate receptors in
1094 one C. elegans interneuron. *Nat Commun*. doi:10.1038/s41467-018-06819-5

1095

1096

1097

Figure list

Figure 1 with 3 supplements

Figure 2 with 1 supplement

Figure 3 with 1 supplement

Figure 4

Figure 5 with 2 supplements

Figure 6 with 2 supplements

Figure 7